Plastic Deformation of Plagioclase in Oceanic Gabbro Accreted at a Slow-Spreading Ridge (Hole U1473A, Atlantis Bank, Southwest Indian Ridge)

Maël Allard, Benoit Ildefonse, Emilien Oliot, Fabrice Barou

JGR Solid Earth

RESEARCH ARTICLE
10.1029/2021JB021964

Special Section:
Ophiolites and Oceanic Lithosphere, with a focus on the Samail ophiolite in Oman

Plastic Deformation of Plagioclase in Oceanic Gabbro Accreted at a Slow-Spreading Ridge (Hole U1473A, Atlantis Bank, Southwest Indian Ridge)

Maël Allard[1], Benoît Ildefonse[1], Émilien Oliot[1], and Fabrice Barou[1]

[1]Géosciences Montpellier, Université de Montpellier, CNRS, Montpellier, France

Key Points:

- Deformation led to the progressive dynamic recrystallization of plagioclase, forming both highly localized and pervasive mylonitic zones
- Dislocation creep produced overall weak crystallographic preferred orientations of plagioclase grains, weakened further in ultramylonites
- The prevalence of the identified active slip systems changes with cooling, during crystallographic preferred orientations development and subgrain boundaries formation

Supporting Information:

Supporting Information may be found in the online version of this article.

Correspondence to:

M. Allard,
mael.allard@umontpellier.fr

Citation:

Allard, M., Ildefonse, B., Oliot, É., & Barou, F. (2021). Plastic deformation of plagioclase in oceanic gabbro accreted at a slow-spreading ridge (Hole U1473A, Atlantis Bank, Southwest Indian Ridge). *Journal of Geophysical Research: Solid Earth*, *126*, e2021JB021964. https://doi.org/10.1029/2021JB021964

Received 27 FEB 2021
Accepted 28 SEP 2021

Abstract Crustal architecture at slow-spreading oceanic ridges results from complex interactions between magmatism, hydrothermalism, and tectonics. IODP Hole U1473A was drilled during Expeditions 360 and 362T at the summit of the Atlantis Bank, a gabbroic massif exhumed at the Southwest Indian Ridge. In this study, we identify and quantify plastic deformation processes in gabbroic lithologies and active slip systems in plagioclase from 115 microstructural domains throughout Hole U1473A. We describe deformed zones using petrographic observations and electron backscattered diffraction analyses made all along the core. Ductile deformation is widespread, and in places strongly localized in mylonitic and ultramylonitic zones. Plagioclase represents ~60% of rock's volume and is the dominant phase accommodating deformation in samples. It shows strong dynamic recrystallization accommodated by subgrain rotation in the dislocation creep regime, forming a fine-grained matrix. Electron backscattered diffraction analyses reveal weak to moderate crystallographic preferred orientations of plagioclase as a result of plastic deformation and strain localization, producing a fabric characterized by (010) parallel to the foliation plane and [100] parallel to the lineation. The fabric strength is first increasing from slightly deformed lithologies to mylonites before decreasing significantly in ultramylonites. This could be explained by orientation scattering after recrystallization, and a change of active slip systems. Subsequent granular flow has likely occurred in some samples. A detailed investigation of intracrystalline misorientations measured at plagioclase subgrain boundaries reveals the activity of four dominant slip systems: [001](010), [100](001), ½[110](001), and ½[$1\bar{1}0$](001). These slip systems reflect decreasing temperatures during CPO development and subgrain wall formation.

Plain Language Summary Crustal architecture of slow-spreading oceanic crust results from complex interactions between magmatism, hydrothermalism, and tectonics. In this study, we identify and quantify plastic deformation processes in gabbroic lithologies and active slip systems in plagioclase from 115 intervals throughout Hole U1473A, drilled at the Atlantis Bank gabbroic massif. We describe deformed zones using petrographic observations, crystallographic orientations analyses, and intragranular deformation analyses made all along the core. Plagioclase represents ~60% of rock's volume and is the dominant phase accommodating deformation in samples. The weak crystallographic preferred orientations measured in plagioclase result from ductile deformation and strain localization. The intensity of crystallographic preferred orientations increases as deformation increases in samples, before decreasing in the most intensely deformed samples. This could be explained by orientation scattering after recrystallization, and a change of active slip systems. Subsequent grain-size-sensitive processes and chemical diffusion have likely occurred in some samples. A detailed investigation of intracrystalline deformations measured in plagioclase grain reveals the activity of four dominant slip systems in addition to the one that produced the crystallographic orientations. These slip systems reflect decreasing temperatures during the deformation of the studied gabbroic lithologies, related to the tectonic activity at the ridge.

1. Introduction

Plastic deformation and recrystallization processes of minerals control the rheological behavior of the lower continental and oceanic crusts during their tectonic history. Deformation of polyphase rocks like granites and gabbros occur over a wide range of temperatures, pressures, strain rates, and fluid conditions. In these rocks plagioclase is ubiquitous, constituting a third to a half of the whole mineralogical assemblage, and is

stable in most crustal conditions (up to ~1–1.5 GPa/~30–40 km, e.g., Newton & Kennedy, 1968). In igneous mafic rocks, plagioclase is the main component and often corresponds to the weaker phase of the mineral assemblage below near-solidus conditions (e.g., Ji, 2004; Kronenberg & Shelton, 1980). Thus, plagioclase plays a key role in crustal rheology, and understanding its mechanical and microstructural behavior is critical (e.g., Rybacki & Dresen, 2004).

In plagioclase grains, internal plastic deformation occurring at high temperatures (>500°–600°C) leads to subgrain rotation (SGR) recrystallization and subsequent (fast) grain boundary migration (GBM) recrystallization (e.g., Drury & Urai, 1990; Kruse et al., 2001; Poirier & Guillopé, 1979; Urai et al., 1986). This usually induces the development of crystallographic preferred orientations (CPO), through dislocation creep, reflecting the activity of syn-deformation slip systems (e.g., Wenk & Christie, 1991). The main slip systems identified by transmission electron microscopy (TEM) observations in plagioclase are those that slip on the principal twin planes, namely (010) and (001), and the most commonly reported one is [001](010) (e.g., Gandais & Willaime, 1984; Montardi & Mainprice, 1987; Olsen & Kohlstedt, 1984).

Slow spreading ridges represent more than 55% of mid-ocean ridges on Earth, and generate about 20% of the global ocean floor (Teagle et al., 2012). At slow-spreading ridges, the development of detachment faults leads to the exhumation of deep crustal and upper-mantle lithologies (e.g., Cannat, 1993), and to the development of oceanic core complexes (OCC; e.g., Escartín & Canales, 2011). OCC are accessible key locations for understanding the relations between high-temperature magmatic processes, cooling, and tectonics occurring at the ridge axis within deep rocks. At the Southwest Indian Ridge, the Atlantis Bank consists of a pluri-kilometer scale gabbro pluton exhumed through an OCC system at 11–13 Ma, and is of great interest for submersible explorations, dredging, and drilling since 1987 (Blum et al., 2017; Dick et al., 2000; Dick, MacLeod, et al., 2019; Pettigrew et al., 1999). Multiple expeditions drilled three deep holes since 1987: ODP Hole 735B (Dick et al., 2000) and Hole 1105A (Pettigrew et al., 1999), and IODP Hole U1473A (Blum et al., 2017; Dick, MacLeod, et al., 2019), for a maximum penetration depth of ~1.5 km. Plastic deformation of the constituting minerals is widespread and penetrative in the uppermost part of the massif (first 500–600 m) before being more heterogeneous and localized down section. The onset of this plastic deformation occurs early in the magmatic accretion history, under hyper solidus conditions, and continues at lower temperature, down to the ductile-brittle conditions. In IODP Hole U1473A, it forms two thick crystal-plastic shear zones at least 100 m large in the upper ~500 m. By contrast, the lower ~300 m show more localized shear zones in a slightly deformed framework (MacLeod et al., 2017).

Our study aims to characterize plastic deformation in gabbroic rocks from the drill core recovered at the Atlantis Bank OCC in IODP Hole U1473A. After reviewing the deformation mechanisms acting in plagioclases in relation with active slip systems, we evaluate the active deformation mechanisms and slip systems and their evolution during cooling in the context of crustal accretion and lower crust–upper mantle denudation through a detachment fault at a slow-spreading ridge. A suite of 102 samples was taken along Hole U1473A in variably plastically deformed gabbroic lithologies; it is characterized by very limited amounts of retrograde alterations and can therefore be used for primary structures analysis. We combine core and thin section observations for textural and mineralogical identifications, and complement these with detailed Electron Backscattered Diffraction (EBSD) mapping.

2. Deformation Mechanisms of Plagioclase

Plagioclase is the most common mineral phase within the Earth's crust, representing up to 40% of crustal minerals (Ronov & Yaroshevsky, 1969). Its pressure-temperature (P-T) stability field encompasses highly variable conditions, which implies that it is subjected to a large spectrum of deformation mechanisms (Figure 1). Activities, and transitions between these mechanisms are controlled by temperature and strain rate, but also by fluids circulation and confining pressure (e.g., Debat et al., 1978; Fitz Gerald & Stünitz, 1993; Hirth & Tullis, 1994; Simpson, 1985; Tullis & Yund, 1987). For $T < 500$°C, plagioclase acts as a rigid mineral and deforms mainly by fracturing. Kink bands, tapered twins, and limited nucleation in small fractures can also be found in fractured grains. The transition between dominant fracturing to dislocation-accommodated deformation occurs at ~450°–550°C in naturally deformed rocks (e.g., Dell'Angelo & Tullis, 1996; Oliot et al., 2010; Tullis & Yund, 1977). The temperature range at which this transition arises also depends on the

texture, and on the constituting phases of the deforming rock (Fitz Gerald & Stünitz, 1993; Ji, 2004; Kronenberg & Shelton, 1980; Rosenberg & Stünitz, 2003; Simpson, 1985; Tullis & Yund, 1977). Dynamic recrystallization and grain boundary migration ("slow" and "fast") become important processes at $T > 500°–600°C$ because of the enhancement of grain boundary mobility, and of subgrain boundary formation at high temperatures. Conversely, at lower temperatures diffusion creep could easily prevail on dislocation creep because of chemical differences accompanying recrystallization (e.g., Rosenberg & Stünitz, 2003). Although dislocation creep does not occur at $T < 500°C$, a process of dislocation generation by fracturing (easy in plagioclase because of twins) is documented and certainly encourages the transition from brittle to plastic regime (McLaren & Pryer, 2001; Stünitz et al., 2003; Tullis & Yund, 1985). Fracturing at moderate to high temperatures (600°–750°C) and high-stress conditions has also been reported as an important process of grain size reduction in plagioclase grains, leading to narrow shear zone formation favoring grain-size-sensitive creep in the small-grained aggregates formed (Okudaira et al., 2015, 2017).

At upper-greenschist to amphibolite facies conditions ($T > 450°C$) the mobility of dislocations in plagioclase becomes easier and promotes their glide toward grain boundaries (Fitz Gerald & Stünitz, 1993). If dislocation mobility is low and local, the nucleation of new grains occurs at grain boundaries by bulging recrystallization (BLG), also known as "slow grain boundary migration," by a process of strain-induced boundary migration (SIGM, Bailey & Hirsch, 1962). Bulges can become (small) new grains by the formation of a subgrain boundary on their back, evolving into a grain boundary (e.g., Bell & Johnson, 1989; Oliot et al., 2014). BLG is mainly observed in plagioclase deformed between 500°–550°C and ~700°C (Figure 1). With increasing mobility dislocations can glide faster and farther, forming subgrains (and then grains) of slightly different crystallographic orientations, or inducing large-scale fast grain boundary migration. The first mechanism, subgrain rotation recrystallization (SGR), occurs in deformed plagioclase from ~400°C to >1000°C, especially in the range 500°–750°C (Figure 1). Grain boundary migration recrystallization (GBM) is made possible by the high mobility of grain boundaries (Poirier & Guillopé, 1979). It is achieved by a rotation step (SGR) that is rapidly followed by the fast migration of the newly formed grain boundary, leading to large recrystallized grain sizes. GBM is naturally active from ~500°C to ~1000°C and is mostly described at 600°–750°C (Figure 1). Note that when SGR and GBM mechanisms are active together, textures are characterized by lobate grain boundaries and small differences in overall grain sizes. Additionally, dislocation creep mechanisms are known to produce CPO, unlike diffusion creep mechanisms (Tullis & Yund, 1987; Wenk & Christie, 1991). In solid solution minerals like plagioclase, slow and fast boundary migration processes can be driven by chemical potentials occurring between neighboring grains (e.g., parent-recrystallized grains). This process is called chemically induced grain boundary migration (CIGM, Hay & Evans, 1987) and arises from a decrease of the P-T conditions. In the dislocation creep regime, the recrystallization of grains by a process of GBM can generate compositional changes in the recrystallized grains. It arises from the migration of the high angle grain boundary within a former strained grain, which permits ionic exchanges (Na/Si and Ca/Al) with the surface of neighboring grains (e.g., Yund & Tullis, 1991). Note that SIGM and CIGM can act simultaneously during grain boundary migration (*s.l.*). By contrast, recrystallization by SGR is not supposed to produce chemical potentials between old and new grains, as the exchanges are principally restricted to volume diffusion, usually too slow to be significant (e.g., Stünitz, 1998; Yund & Tullis, 1991).

Slip systems activities during intracrystalline deformation are documented from ~500°C to 600°C to higher temperatures up to the solidus (Figure 1). Numerous slip systems have been specified after experimental deformations since the seventies (e.g., Marshall & McLaren, 1977; Montardi & Mainprice, 1987; Olsen & Kohlstedt, 1985; 1984; Scandale et al., 1983), and observed in TEM. These studies raised the general idea that slip by dislocation motion is one of the main deformation mechanisms in feldspars. Furthermore, cross slip is commonly observed and the interaction between several operating slip systems is considered as an important mechanism for dislocation multiplication (e.g., Montardi & Mainprice, 1987). An exhaustive list of slip systems documented in plagioclase to date is presented in Table S1 in Supporting Information S1.

Based on TEM studies and CPO pattern interpretations, it appears that the main active slip systems are characterized by a slip plane that corresponds to a twinning plane, namely (010) or (001). Apart from [001](010) that is found active from ~500°C and over the largest range of temperatures, most slip systems become active at ~600°C and are well documented until 900°C (Figure 1). [100](010) is one of the dominant active slip systems at high temperatures (>800°C) while the [100](001) slip system, found active in the same range

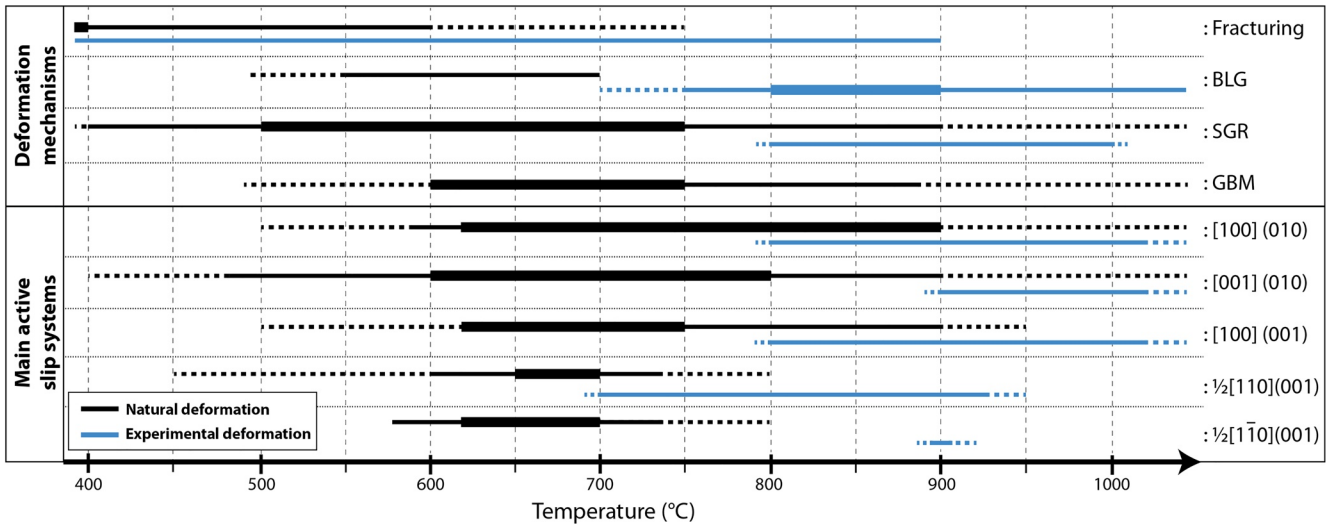

Figure 1. Plagioclase deformation mechanisms and most reported slip systems activities, plotted as a function of the temperature, for natural (black) and experimental deformations (blue). BLG: bulging recrystallization; SGR: subgrain rotation recrystallization; GBM: fast grain boundary migration recrystallization (see references in the text). GBM is not described in experimentally deformed plagioclase. The increasing importance of a deformation mechanism (or a slip system activity) is represented by the increasing thickness of the line. The full list of used references is given in Table S2 in Supporting Information S2.

of temperatures, is less documented at high temperatures. When both [001](010) and [100](010) slip systems are observed simultaneously active, a switch of prevalence from the [001] to the [100] direction seems to occur at ~800°C. Finally, the <110>(001) family of slip systems has been observed in a restricted range of temperatures, principally from ~600°C to 750°C. In anorthosites and gabbros, the preferred orientation of (010) is commonly interpreted as defining a foliation plane formed as a result of magmatic flow that preferentially aligns tabular plagioclase crystals (e.g., Benn & Allard, 1989; Ji et al., 2014; Satsukawa et al., 2013).

3. Geological Setting and IODP Hole U1473A

The ultraslow-spreading Southwest Indian Ridge (SWIR) has a full spreading rate of ~14 mm/yr (e.g., Hosford et al., 2003). Located 79–116 km south of the ridge axis, the Atlantis Bank (32° 42.3622′S, 57° 16.6880′E) is a pluri-kilometric gabbroic pluton bordered on its western flank by the north-south Atlantis II Transform (Figure 2a). This massif is an OCC exhumed by detachment faulting at 11–13 Ma. Lying at 700 m below sea level, the summit of the Atlantis Bank is a flat surface corresponding to a wave-cut platform, eroded ~9.5 Ma ago (Figure 2a, Dick et al., 1991). Although the surface of the Atlantis Bank is not a typical detachment surface, the presence of talc-serpentine schists around the massif is documented (e.g., Baines et al., 2003; Dick, Kvassnes, et al., 2019), as well as low-angle dipping ductile shear zones located in the upper parts of ODP Hole 735B and IODP Hole U1473A (Dick et al., 2000; Dick, Kvassnes, et al., 2019). These shear zones predominantly display normal sense of shear in the upper 50 and ~450 m of holes U1473A and 735B, respectively, before becoming reverse at greater depths (Dick, MacLeod, et al., 2019).

IODP Hole U1473A was drilled from the summit of the Atlantis Bank to 809.4 m below seafloor (mbsf) during IODP Expeditions 360 and 362T (Blum et al., 2017; Dick, Kvassnes, et al., 2019). The two other holes drilled between 1987 and 1998, are located 1–2 km away from Hole U1473A: ODP Hole 735B (1508 mbsf, Dick et al., 2000) and ODP Hole 1105A (158 mbsf, Pettigrew et al., 1999). Sections recovered from these three holes consist of olivine-gabbros with minor oxide (-bearing) gabbros, gabbros, and troctolites (Figure 2b, Dick et al., 2000; Pettigrew et al., 1999).

In gabbroic lithologies from Hole U1473A, ductile deformation is frequent, particularly in the upper 500 mbsf. This upper section displays porphyroclastic to protomylonitic textures, in which meter-scale ultramylonites zones are common (Figure 2c). Two important and near-continuous zones of intense crystal-plastic deformation are located between 150 and 250 mbsf, and between 300 and 400 mbsf (MacLeod et al., 2017). The deeper part of Hole U1473A (from 500–600 to ~800 mbsf, Figure 2c) is affected by

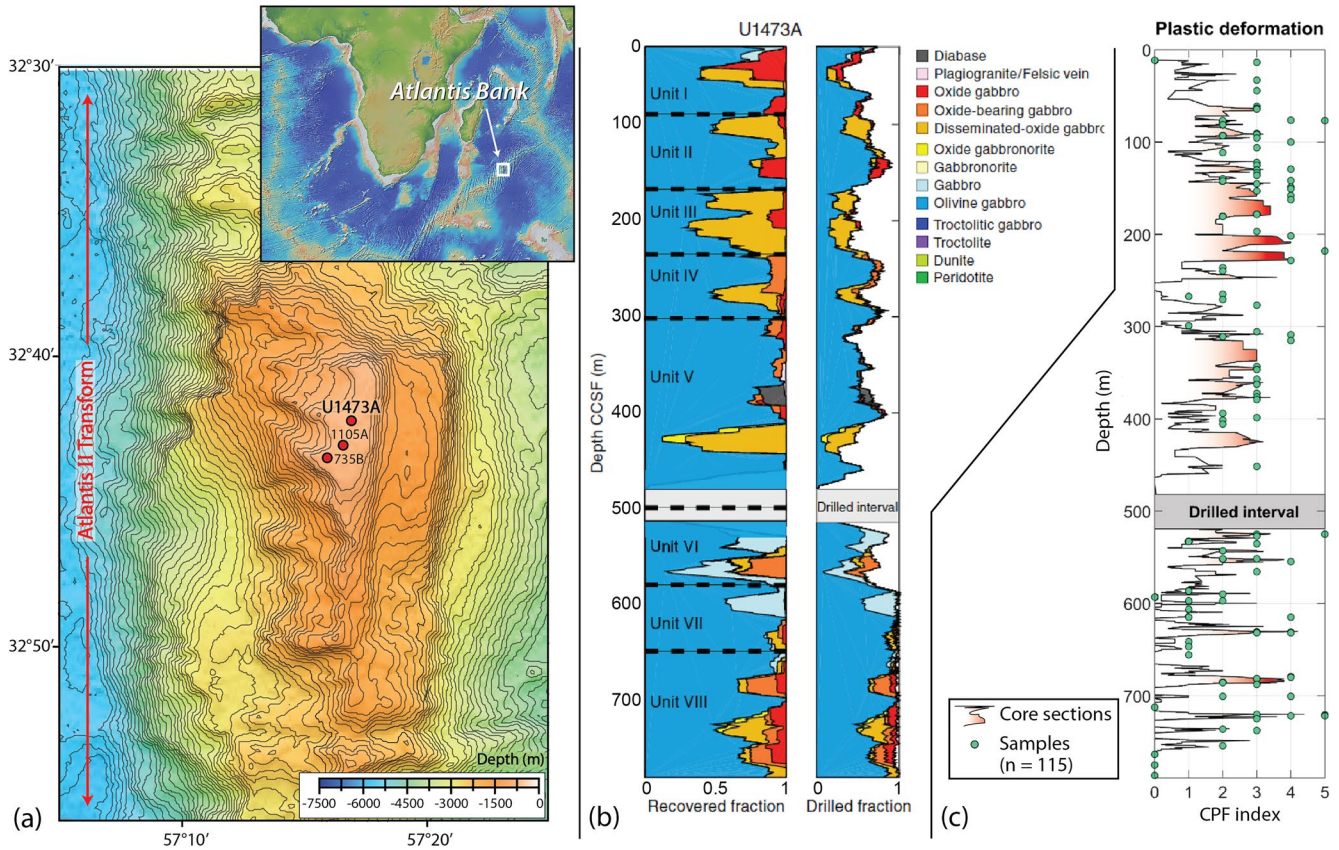

Figure 2. Location and characteristics of interests of Hole U1473A. (a) Bathymetric map of the Atlantis Bank, modified after Dick et al. (2017). The inset displays the location of the Atlantis Bank at the SWIR (Ryan et al., 2009) ; (b) Lithologies from Hole U1473A, after MacLeod et al. (2017); (c) Moving average of the apparent deformation intensity (crystal plastic fabrics (CPF)) inferred from macroscopic core observations (running average on five depth intervals, see MacLeod et al., 2017), and position along the depth of all studied samples with their CPF index. The drilled interval (481.7–519.2 mbsf) was drilled without coring. The red color below the curve highlights the deformed zones. CPF index: 0 = undeformed, 1 = foliated, 2 = porphyroclastic, 3 = protomylonitic, 4 = mylonitic, 5 = ultramylonitic. "n" is the number of analyzed depth intervals.

more localized ductile deformation, with thin high-strain zones that are heterogeneously distributed in a framework of undeformed to porphyroclastic gabbroic lithologies. These shear zones are centimeter-scale ultramylonites to rare meter-scale mylonites. Shipboard observations reveal that 42% of the core presents preserved magmatic textures. The qualitative categorization of crystal-plastic fabrics (CPF), ranging from 0 to 5 (CPF index: 0 = undeformed, 1 = foliated, 2 = porphyroclastic, 3 = protomylonitic, 4 = mylonitic, 5 = ultramylonitic), shows that deformed zones are characterized by 32% of porphyroclastic to protomylonitic textures, and 13% of mylonitic to ultramylonitic textures (Figure 2c, MacLeod et al., 2017).

The whole ductile deformation history within the Atlantis Bank appears to have occurred continuously from hyper-solidus conditions to lower temperatures while successive igneous gabbroic intrusions were emplaced. This is described as a process of dynamic accretion, characteristic of slow-spreading ridges with low to intermediate magmatism (Dick, MacLeod, et al., 2019).

Conditions for ductile deformation at the Atlantis Bank result in multiple deformation stages. Two dominant types of deformation are identified: solid-state deformation through dislocation creep, and melt-assisted deformation through both melt-rock reactions and dislocation creep. A first stage of solid-state deformation (Stage 1) led to the recrystallization of former igneous plagioclase, pyroxenes, and olivine grains. It is documented at 907°–1093°C (median = 1026°C; Gardner et al., 2020) and ~860°–940°C (Mehl & Hirth, 2008) in Hole 735B, at 862–910°C in submersible samples from the Atlantis Bank surface (Miranda & John, 2010). Following this initial solid-state deformation stage, two melt-assisted deformation episodes are reported in the presence of melt (grouped in Stage 2). The first episode (Stage 2a) occurred at 846°–969°C (median at 949° and 906°C; Gardner et al., 2020), and the second (Stage 2b) at 817°–1000°C, mainly from ~800 to 900°C

(Gardner et al., 2020; Taufner et al., 2021). A lower temperature solid-state event (Stage 3) is documented in mylonites at 740°–840°C (median at 780°C in Miranda et al., 2016, and 795°C in Miranda & John, 2010). An ultimate stage of solid state–semi-brittle deformation (Stage 4) is recorded mainly in plagioclase-amphibole bearing mylonites/ultramylonites at 665 ± 40°C (Miranda & John, 2010).

4. Methods

A collection of 102 gabbroic rock samples (115 microstructural domains) were taken for this study between 11.3 and 786.5 mbsf (average spacing of 6.8 m, Figure 2c) in Hole U1473A, targeting intervals with crystal-plastic deformation. These studied microstructural domains are mainly attributed to a continuum of deformation from early Stage 1 to Stage 3 under solid-state conditions. Some highly deformed domains display textural similarities with domains associated to stage 2 deformations. Some of the studied mylonites and ultramylonites may have undergone deformation in the presence of melt. Finally, the plagioclase-amphibole ultramylonites formed during late Stage 4. Core sections were split onboard to maximize the expression of dipping structures on the cut face (e.g., foliation) while maintaining representative features in both core section halves (MacLeod et al., 2017). Hence the plane of analysis is orthogonal to the foliation, and the lineation is generally not known but is deduced from the plagioclase CPO. Sample names (I_II_III) indicate the core number (I), the number of the section in the core (II), the top depth in the section in cm (III). A letter (A, B, or C) identifying the microstructural domain is added at the end when several domains were analyzed at the same depth or in the same sample.

4.1. EBSD Analyses

Crystallographic analyses were performed with the electron backscatter diffraction (EBSD) technique, using the CamScan X500FE Crystal Probe SEM, equipped with the Oxford instruments Nordlys®, and later on, Symmetry® EBSD detector, and the Jeol 5600 SEM equipped with the Oxford instrument NordlysNano EBSD detector at Geosciences Montpellier lab. The diffraction pattern acquisition was achieved at a working distance of 25 mm, an indexing speed of 140 Hz, an acceleration voltage of 20 kV, and a probe current of 10 nA. The scanning resolution was chosen as a function of the mean minimum grain size of each analyzed sample and finally varies from 2.5 to 30 μm (average resolution: 10 μm). The indexing rate is relatively high on raw maps ranging from 73% to 98%, with a large majority of samples around 90%. Thin section mapping was generally done on areas of 1–2 cm^2, and on whole thin sections for the five coarse-grained samples considered in this study.

4.2. EBSD Data Processing

Data processing was performed on 115 microstructural domains with the MTEX Matlab® toolbox (version 5.3.1, e.g., Mainprice et al., 2015), to calculate pole figures, inverse pole figures (IPF), and parameters indicative of the fabric strength: the J index and pole figure index PfJ, derived from the orientation density function (ODF), and the M index derived from uncorrelated misorientations. J varies from one for random orientations to infinity for a single orientation (e.g., Bunge, 1982). PfJ is expressed as an integral of the ODF, calculated for a unit axis given in crystal coordinates and a unit direction in specimen coordinates, and varies the same way as J index (e.g., Mainprice et al., 2015). M index is defined as the difference between the distribution of measured uncorrelated misorientation angles and the distribution of uncorrelated misorientation angles of a random fabric, and varies from zero for a random fabric to one for a single orientation fabric (Skemer et al., 2005). Calculated parameters for each analyzed sample are given in Table S3 in Supporting Information S2.

Only pixels with mean angular deviations (i.e., the angle between the acquired diffraction pattern and the indexing solution) below 1°, and grains containing more than five pixels have been considered in data sets. The grain segmentation angle used is 10°. Misorientations lower than 2° between two neighboring pixels have not been considered (Trimby et al., 1998). Average grain orientations were used for calculation of pole figures and orientation parameters, instead of the pixel orientation data set, in order to give equivalent weights to all grains, regardless of their size. The twinned plagioclase grains are reconstructed by identifying the twin boundaries and merging twinned domains within a same grain for grain orientation analysis.

Twins are identified from their boundary angle (>175°) and a rotation in (010) and (001), and around [010] and [001]. The orientation of the largest twin domain is attributed to the reconstructed grain.

Recrystallized grains were automatically selected using the following parameters: (a) a grain orientation spread (GOS) <2°, which corresponds to the average of the misorientations between each pixel in a grain and the grain mean orientation (e.g., Brewer et al., 2009); (b) a tortuosity <1.4 (ratio between the grain perimeter and the convex hull perimeter); and (c) an equivalent diameter <700 μm (diameter of a circle of the same area as the grain). These threshold values were chosen due to their good reproducibility in the sample suite, and give a lower bound for the amount of recrystallization in samples. Calculated recrystallized fractions were then systematically optically checked to prevent possible errors. EBSD maps also allowed us to calculate the phase modal amounts in each analyzed domains. In the following, medians and interquartile ranges (i.e., the interval between the first and third quartiles of a data set) are used to evaluate the evolution of the recrystallized fraction in analyzed microstructural domains with increasing deformation.

4.3. Misorientations Analysis

The deformation of grains and their recrystallization results in orientation relations characterized by specific rotation axes and associated rotation angles, known as misorientations (e.g., Wheeler et al., 2001). The misorientation axis and angle distributions between porphyroclasts and their neighboring recrystallized grains, indicative of the deformation mechanism, have been measured (e.g., Jiang et al., 2000; Kruse et al., 2001; Svahnberg & Piazolo, 2010). The rotation axes of misorientations measured within grains are used to determine the type of subgrains (e.g., tilt or twist) and the possible slip systems having produced these misorientations (e.g., Lloyd et al., 1997). The analysis of correlated and uncorrelated misorientation angle distribution is performed after the twin boundaries have been merged into their host grain to focus on other boundaries. Another misorientation parameter use is the GOS, which is the average of the deviation between the orientations of pixels within a grain from the mean orientation of the grain.

Plagioclase slip planes (010) and (001) can be considered as the easiest slip planes in the sense that they intersect the smallest number of tetrahedra-O bonds of the framework structure (Gandais & Willaime, 1984; Ji et al., 1988; Tullis, 1983). In order to look at active slip directions on these planes, we selected in each analyzed domains two groups of grains: one with (001) parallel to the analyzed plane of the thin section (plane orthogonal to Z), and a second for (010) being parallel to the analyzed plane. A tolerance angle of 15° was arbitrarily taken. Misorientation rotation axes observed in these planes indicates the type of dislocation associated with the measured misorientations: edge dislocations if they belong to the selected plane and screw dislocations if they are orthogonal to it. The burgers vectors of these dislocation systems can then be deduced from the orientation relationship between the misorientation axis, the inspected plane, and the structural orientation. Then, as explained in Kruse et al. (2001) we will consider a slip system to be well orientated for glide if its Burgers vectors is close to the lineation and within the foliation plane. The plagioclase structure is assumed to be $C\bar{1}$ due to their compositional range varying from andesine to labradorite and to their thermal context (Smith, 1984).

5. Sample Descriptions

Analyzed microstructural domains (115 on 102 samples) consist of 70 olivine gabbros, 14 oxide gabbros (oxide content >1%), 13 olivine oxide gabbros, 8 gabbros, 3 gabbronorites, 3 oxide gabbronorites, 2 amphibolitic metagabbros, 1 anorthosite, and 1 oxide gabbronorite. The average mineralogical assemblage in all lithologies consists of plagioclase (Pl, ~50%), clinopyroxene (Cpx, ~30%), subordinate olivine (Ol, ~5–10%) and orthopyroxene (Opx, ~2–5%), and minor oxides (Ox) and amphiboles (Amph, Table S3 in Supporting Information S2). Microstructural evolutions occur without significant petrological changes, with relatively constant average modes of plagioclase. Conversely, modes of clinopyroxene and olivine decrease as the deformation increases in samples, from 27%–30% to ~20% in clinopyroxene and from ~10% to the disappearance of olivine. This is accompanied by a rise of amphibole modes (~3%–~14%) and of orthopyroxene (~1.5%–~5%).

Alteration is weak in the selected sample suite, principally associated with veinlets and almost exclusively restricted to the upper half of Hole U1473A. These veinlets, mainly filled by green amphiboles, rarely by

chlorite, are observed in 31 samples located in the upper 570 mbsf. The veinlets are orthogonal to the trace of the foliation in 22 samples and oblique in the others.

Plagioclase found in Hole U1473A gabbroic lithologies has a composition ranging between andesine and labradorite (An_{36} to An_{71}), with more An rich compositions in gabbros and olivine-gabbros (An_{40} to An_{71}) than in oxide-bearing-gabbros (An_{36} to An_{45}, Dick, Kvassnes, et al., 2019; Nguyen et al., 2018; Nozaka et al., 2019). A decrease of 2%–3% in An content is measured from the core to rims in some samples, as well as in partially albitized gabbros where it decreases to An_{32} (Nozaka et al., 2019). Clinopyroxene is augite; its Mg# varies from 0.48 to 0.86 with a mean at 0.74 in gabbros and olivine-gabbros, and 0.70 in oxide-bearing-gabbros (Dick, Kvassnes, et al., 2019; Nguyen et al., 2018; Nozaka et al., 2019). The Mg# of olivines varies from 0.46 to 0.80 in all gabbroic rocks (Dick, Kvassnes, et al., 2019; Nguyen et al., 2018; Nozaka et al., 2019). Orthopyroxene is hypersthene, and has a Mg# varying from 0.56 to 0.79, with a mean at 0.67 (Dick, Kvassnes, et al., 2019; Nozaka et al., 2019).

One hundred and seven analyzed microstructural domains (over 115) are plastically deformed, and 72 corresponds to CPF indices 3 to 5 (protomylonites to ultramylonites). Dynamic recrystallization of plagioclase, clinopyroxene, and olivine is the main deformation accommodation mechanism observed within the studied domains (Figure 3). Recrystallized minerals constitute at least 50% of modes in a majority of the analyzed domains (Figure 4). Accordingly, core and mantle structures around magmatic porphyroclasts are widespread, and nucleation bands in grains-scale fractures or thin section-scale fractures occur in plagioclase. In the following sections, deformation mechanisms are identified by both optical observations and EBSD analyses.

5.1. Undeformed Domains (CPF Index 0, Figure 3a)

Microstructural domains with no apparent (or very limited) plastic deformation varies from fine to coarse grained. Textures are generally granular in fine-grained domains (~100–150 μm) with subequant grain shapes, and subophitic in coarse-grained domains (0.5 mm–1.5 cm) with laths of subhedral plagioclases that penetrate pyroxenes oikocrysts, and anhedral olivine (Figure 3a). In these microstructures the analyzed domains consist of five olivine gabbros, two olivine oxide gabbros, and 1 gabbronorite. The mineralogical assemblage contains on average plagioclase (59.2%), clinopyroxene (27.1%), olivine (10.8%), orthopyroxene (2.0%), and minor amphiboles and oxides (<1%). Plastic deformation is not completely absent, as indicated by limited undulatory extinction in plagioclase, clinopyroxene, and olivine crystals, sometimes accompanied by tapered twins in plagioclase (Figure 3a). Grain boundaries are straight or lobate. A magmatic foliation is observed in fine-grained granular domains through the discrete shape preferred orientation of plagioclase and clinopyroxene grains. This is not observed in domains of coarser grain sizes, possibly because of the limited number of grains at thin section scale.

5.2. Foliated Domains (CPF Index 1, Figure 3b)

The original subophitic or granular texture is partly preserved in the foliated domains; only a limited amount of deformation is accommodated by pyroxene and olivine, and the grain size is medium (0.1–0.5 cm, Figure 3b). In these microstructures the analyzed domains consist of eight olivine gabbros, one oxide gabbro, and 1 gabbro. These lithologies contain on average plagioclase (60.9%), clinopyroxene (30.2%), olivine (4.0%), amphibole (3.3%), orthopyroxene (1.6%), and minor oxides (<1%). Plagioclase porphyroclasts (Pl_1; see Figure 5) show undulatory extinction and some subgrain boundaries, tapered deformation twins, grain boundary migration, and grain boundaries are lobate and sometimes serrated (e.g., Figures 5a and 5d). Dynamic recrystallization is ~40% of the whole mineral assemblage (Figure 4a) and the calculated fractions of recrystallized plagioclase (Pl_2), 44%, are positively skewed with an IR = 42.2% (the median is closer to the first quartile than to the third one, Figure 4b). The grain size of Pl_2 grains is variable (50–250 μm), on average ~140 μm. Deformation is largely accommodated by plagioclase and leads to the loss of the lath shape of primary plagioclase and the formation of inequigranular aggregates of recrystallized Pl_2 grains (Figure 3b).

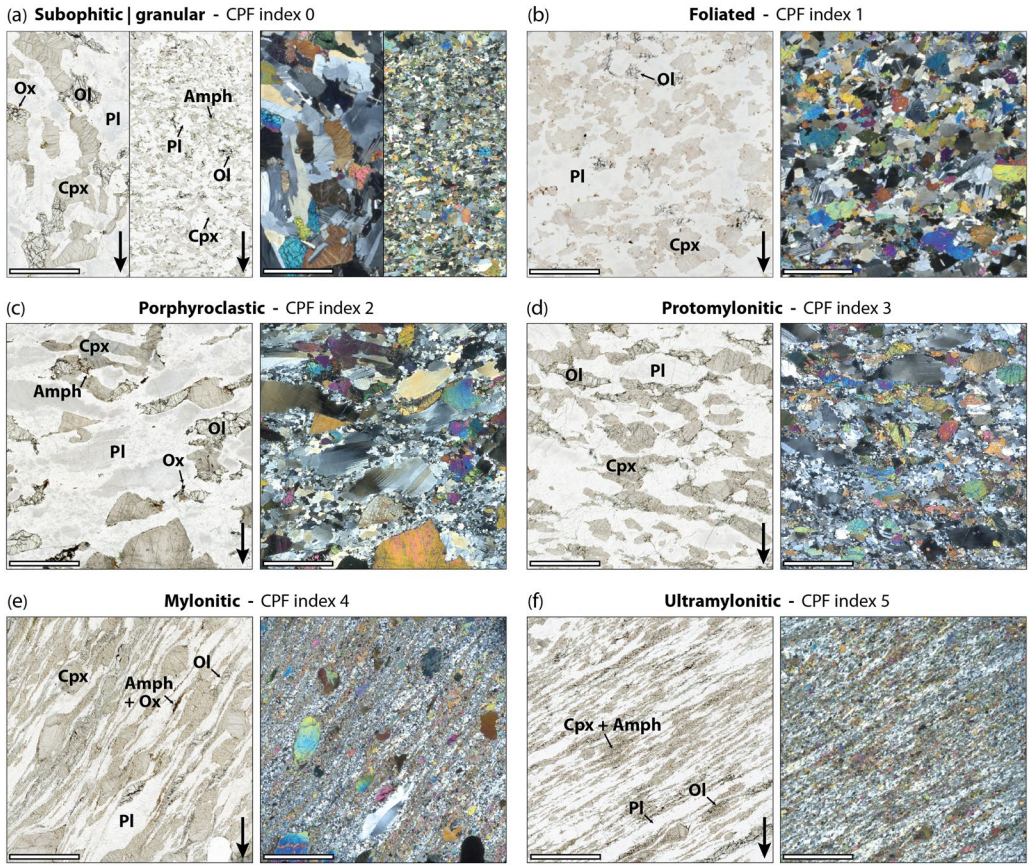

Figure 3. Representative microstructures observed in studied intervals from Hole U1473A. (a) Undeformed subophitic microstructural domain 88_5_117 and granular domain 66_1_96; (b) Foliated domain 70_7_6; (c) Porphyroclastic domain 13_2_59; (d) Protomylonitic domain 50_2_43; (e) Mylonitic domain 69_5_73_A; (f) Ultramylonitic domain 58_5_79_C. In each subfigure sections, on the left are plane-polarized light microphotographs, and on the right cross-polarized light microphotographs. The scale bar length is 5 mm. The bottom-right arrows indicate the down hole direction in the rock. Pl: Plagioclase; Cpx: Clinopyroxene; Ol: Olivine, Amph: Amphibole, Ox: Oxide.

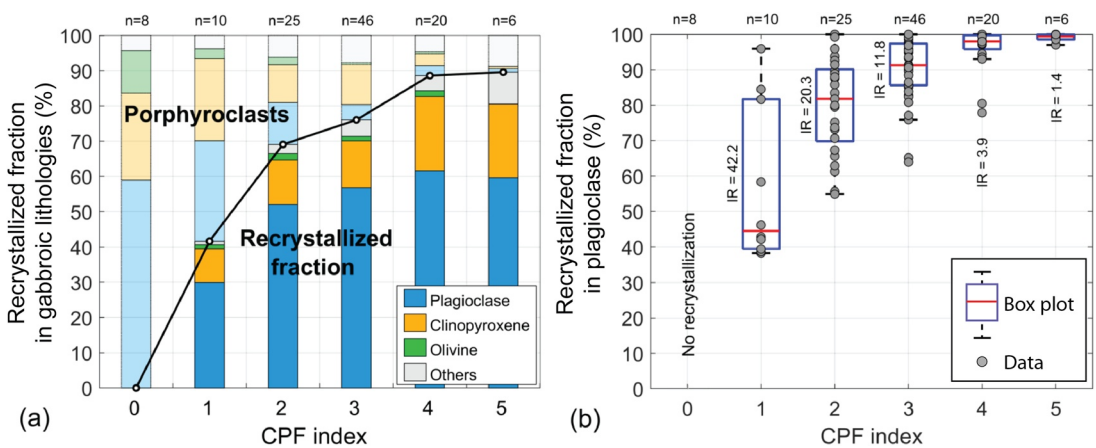

Figure 4. Modal proportions of recrystallized minerals deduced from EBSD maps and plotted as a function of the CPF indices of microstructural domains. (a) Evolution of the recrystallized fraction in studied domains (black curve) and superimposed cumulative histograms of recrystallized fractions (bottom) and porphyroclast fractions (top, translucent) within main constitutive phases. "Others" correspond to orthopyroxene, oxide, and amphibole. All values are medians of normal distributions, and "*n*" is the number of analyzed microstructural domains. (b) Boxplots showing the proportions of the recrystallized fraction in plagioclase. "IR" is the interquartile range of the data set. Blue boxes contain 50% of the data located between the first (25%) and third (75%) quartiles. The red line is the median value and the whiskers (dotted line) extend within ±2.7 σ for normally distributed data sets. Data points outside of the whiskers are not considered.

5.3. Porphyroclastic Domains (CPF Index 2, Figure 3c)

The original subophitic or granular texture is lost in porphyroclastic domains. Recrystallization of plagioclase and olivine grains induces the development of millimeter-sized, weakly foliated porphyroclastic aggregates forming core and mantle structures (Figures 3c, 5d and 5f). Clinopyroxene recrystallizes from its edges, but to a lesser extent than in plagioclase and olivine (Figure 3c). In these microstructures the analyzed domains consist of 20 olivine gabbros, 2 oxide gabbros, 1 olivine oxide gabbro, 1 oxide gabbronorite, and 1 anorthosite. Mineral proportions are on average plagioclase (66.5%), clinopyroxene (22.4%), olivine (5.7%), amphibole (2.6%), orthopyroxene (2.1%), and minor oxides (<1%). Pl_1 grains display tapered twins, grain boundary migration, frequent undulatory extinction, and subgrain boundaries (Figure 5a, 5d and 5f). Pl_1 grain boundaries are usually serrated, sometimes lobate. Pl_2 grain size usually ranges from 70 to 100 μm (median = 89 μm). Pl_2 grain boundaries are often lobate, and tapered twins are common. Grain boundary migration and undulatory extinction are often found in olivine grains (Figure 5b). Recrystallization rises to ~70% overall (Figure 4a) and is ~82% in plagioclase (Figure 4b). In these textures, the recrystallized fraction distribution is negatively skewed (median close to the third quartile) with a high IR (20.3%).

5.4. Protomylonitic Domains (CPF Index 3, Figure 3d)

In protomylonitic textures, plagioclase tends to be highly recrystallized and forms a connected fine-grained matrix in which magmatic clinopyroxene and olivine porphyroclasts continue to dynamically recrystallize from their edges (Figure 3d). The foliation is well defined by recrystallized aggregates of clinopyroxenes and olivines, and elongated porphyroclasts of plagioclases and clinopyroxenes (Figure 3d). In these microstructures the analyzed domains consist of 24 olivine gabbros, 8 oxide gabbros, 8 olivine oxide gabbros, 5 gabbros, and 1 olivine oxide gabbronorite. The mineralogical assemblage contains on average plagioclase (63.1%), clinopyroxene (23.2%), amphibole (5.1%), orthopyroxene (3.2%), olivine (3.1%), and oxides (~2%). Pl_1 grain boundaries are mostly serrated, whereas the Pl_2 grain boundaries are lobate or curvilinear. Both frequently contain tapered deformation twins. Subgrain boundaries in Pl_1 porphyroclasts are widespread, and sometimes present in large Pl_2 grains (200–300 μm, e.g., Figure 5d). Some microstructural domains display minor evidence of grain boundary migration forming small new grains (10–20 μm) closed by subgrain boundaries, while others are indicative of static recrystallization microstructures in plagioclase grains (Figures 5g and 5h). Subgrain boundaries are found in olivine grains, and in recrystallized clinopyroxene aggregates occurring together with grain boundary migration (Figure 5c, 5e and 5f). The Pl_2 grain size ranges from 50 to 100 μm (median = 69 μm). Recrystallization reaches ~75% overall (Figure 4a) and ~91% in plagioclase (Figure 4b). Recrystallized fractions of plagioclase are normally arranged and the IR is low (IR = 11.8%, Figure 4b).

5.5. Mylonitic Domains (CPF Index 4, Figure 3e)

A strong foliation characterizes mylonitic domains due to the dynamic recrystallization of an important fraction of clinopyroxene and olivine, in addition to plagioclase, in elongated sigmoid aggregates (Figure 3e). This foliation consists of alternating plagioclase-rich and clinopyroxene-rich slightly undulating bands. In these microstructures the analyzed domains consist of 12 olivine gabbros, 2 oxide gabbros, 2 olivine oxide gabbros, 2 oxide gabbronorites, 1 gabbronorite, and 1 amphibolitic metagabbro. The mineralogical assemblage is on average plagioclase (61.7%), clinopyroxene (23.3%), amphibole (6.2%), orthopyroxene (4.3%), olivine (2.9%), and others including oxides (<2%). Pl_2 grain boundaries are mostly curvilinear while Pl_1 grain boundaries are mostly serrated. Tapered twins and subgrain boundaries are common in grains larger than 0.5 mm. The recrystallized fraction is ~88% (Figure 4a) and rises to ~97% in plagioclase (Figure 4b). Data are normally arranged and associated with a low IR (IR = 3.9%, Figure 4b). The Pl_2 grain size is 30–70 μm (median = 52 μm) and decreases to 10–20 μm in localized shear bands (e.g., Figure 5e).

5.6. Ultramylonitic Domains (CPF Index 5, Figure 3f)

Ultramylonitic textures are characterized by an almost complete dynamic recrystallization of all grains and a straight layering formed by nearly continuous plagioclase-rich bands that alternate with clinopyroxene-rich bands (Figure 3f). In these microstructures the analyzed domains consist of 2 gabbros, one olivine

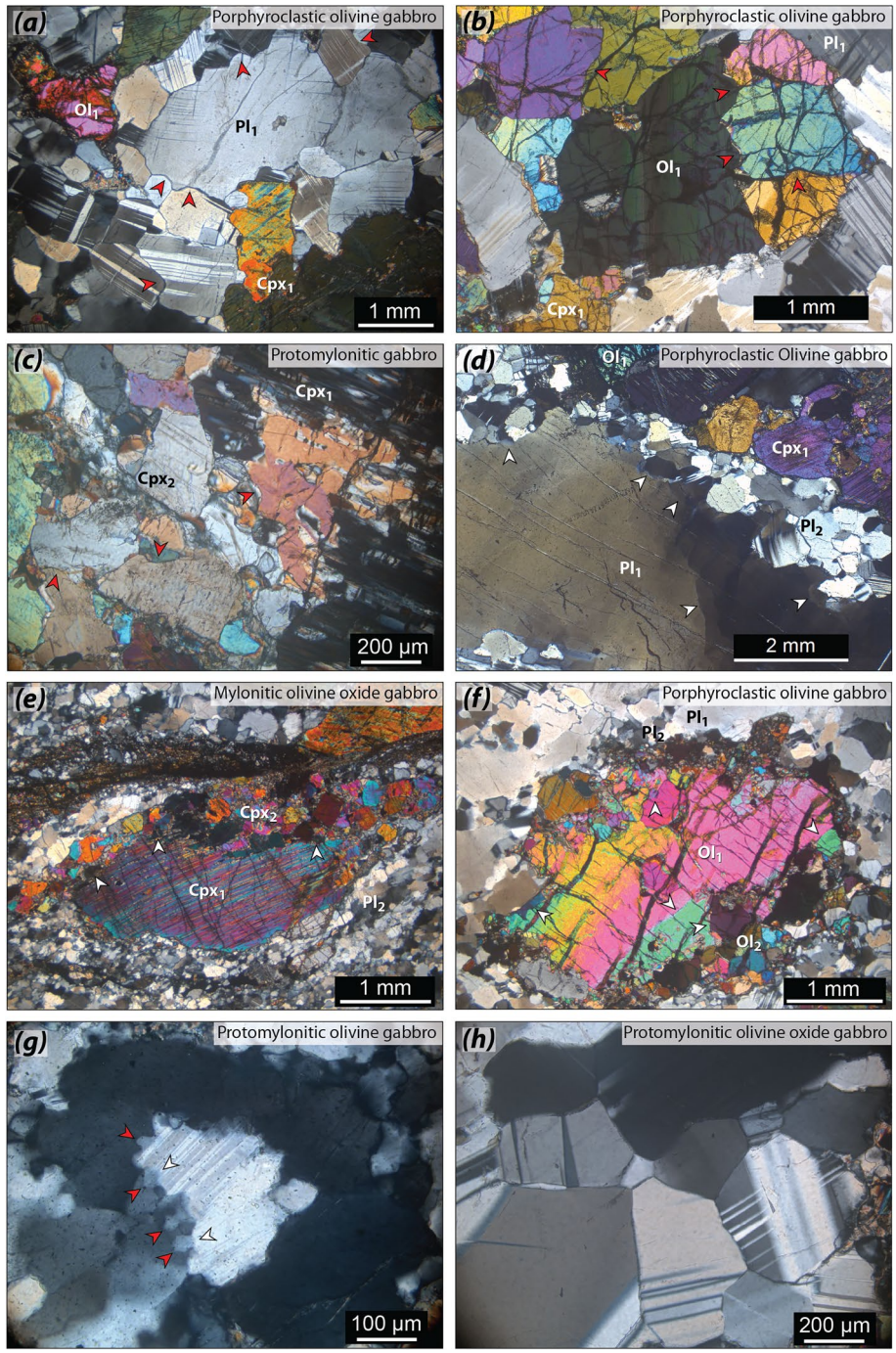

Figure 5. Cross-polarized microphotographs of representative microstructures and recrystallization mechanisms, observed in studied intervals from Hole U1473A. (a–c) Evidence of grain boundary migration in (a) plagioclase (Pl), (b) olivine (Ol), and (c) clinopyroxene (Cpx). The indices "1" and "2" indicate primary grains and recrystallized grains, respectively. Red arrows indicate boundary migration. Note the frequent occurrence of tapered twins in plagioclase grains. (d–f) Evidence of subgrain rotation recrystallization in (d) plagioclase, (e) clinopyroxene, and (f) olivine, forming core and mantle structures. Note that parent grains display undulatory extinction. White arrows indicate subgrain boundaries. (g) Evidence of bulging recrystallization in plagioclase forming a core and mantle structure. Note that most of the bulges are closed by a subgrain boundary (white arrows). (h) Polygonal fabric and related 120°-triple junctions of plagioclase, testifying for static recrystallization. Note the systematic occurrence of tapered twins.

gabbro, one oxide gabbro, 1 gabbronorite, and 1 amphibolitic metagabbro. The mineralogical assemblage contains on average plagioclase (59.1%), clinopyroxene (20.4%), amphibole (14.4%), orthopyroxene (5.3%), and minor olivine and retrograde phases (other than amphibole; <1%). Pl_2 grains have lobate to serrated boundaries, and tapered deformation twins and subgrain boundaries are frequent. Ultramylonitic deformation is frequently highly localized at a very small scale (from 0.5 mm to 1–2 mm thick bands), although it can occur at the pluri-decimeter scale (as in sample 58_5_79_C, Figure 3f). Recrystallization reaches ~90% overall (Figure 4a) and is complete in plagioclase (Figure 4b), with a very low IR (IR = 1.4%, Figure 4b). The size of Pl_2 grains ranges from 15 to 30 μm (median = 21 μm), and sometimes 5–10 μm in shear bands.

6. EBSD Analysis of Plagioclase

6.1. Crystallographic Preferred Orientations

In the undeformed (CPF index 0) and foliated (CPF index 1) microstructural domains, misorientation maps indicate little intra-grain deformation (e.g., Figure 6a). In undeformed microstructures, CPO are generally random in coarse-grained domains and can be strong in fine-grained domains (Figures 6a and 7a). Note that the number of analyzed grains in coarse-grained domains is not statistically significant; hence the resulting CPO is not necessarily representative of the sampled domain. In fine-grained undeformed domains, the foliation is parallel to the preferred orientation of plagioclase (010) planes, accompanied by an orthogonal girdle (rarely a point maximum) of [100] axis, which aligns in the magmatic foliation (Figures 6a and 7a). The foliation and the preferred orientation of plagioclase (010) are generally sub parallel, so the preferred orientation of (010) in plagioclase is used in pole figures as a proxy to the foliation (pink great circles, Figures 6a and 7a). Foliated domains (CPF index 1) display similar CPO patterns as fine-grained undeformed domains with a weaker fabric strength (Figure 7b).

The increase of plastic deformation results in progressive recrystallization (Figures 3 and 4), especially in plagioclase, accompanied by the widespread development of subgrain boundaries in grains (Figures 6d and 6e). These subgrains first form in porphyroclasts (CPF indices 2 and 3, Figures 6b and 6c), but as deformation progresses, they also develop in the larger recrystallized grains (CPF indices 4 and 5, Figure 6c–6e). From CPF indices 2 to 5, typical CPO has (010) lying close to the foliation plane and [100] aligned in this plane (Figures 6b–6e, and 7c–7f). Point maxima are most common for both (010) and [100], although girdle distributions can be found. (001) commonly forms girdles orthogonal to the foliation. Seven protomylonitic to ultramylonitic domains (CPF indices 3 to 5) show an alignment of (001) close to the foliation rather than (010) (e.g., Figures 7d and 7f, samples 6_2_128 and 81_6_117_B). In all analyzed domains, the transition from porphyroclastic to mylonitic samples (CPF indices 2 to 4) is accompanied by the development of a lineation well-defined by the preferred alignment of [100] (Figures 6 and 7).

Considering the parent-child grains relationships, we observe in porphyroclastic to mylonitic domains (CPF indices 2 to 4) a strong similarity in crystallographic orientations (e.g., Figures 6b and 6c). It is referred to as a "host-controlled" orientation of recrystallized grains. Among the 88 analyzed microstructural domains containing porphyroclasts (CPF indices 1 to 5), 52 domains display similar CPO patterns in porphyroclasts and recrystallized grains, and the preferred orientations of at least [100] and (010) are similar in 63 domains (e.g., Figures 6b and 6c). The CPO patterns display no similarities between porphyroclasts and recrystallized grains in only 16 domains.

All studied domains through IODP Hole U1473A show relatively weak CPO as indicated by low values of J and M indices, usually below 3 and 0.09 respectively (Figures 8a and 8b). The evolution of the CPO strength as a function of the CPF index is significantly different for the two strength indices. Median J values indicate a smooth decrease of CPO strength from ~3.0 in CPF index 0 to ~1.8 in CPF index 5, passing through ~2.3 in CPF index 2 (Figure 8a). High IR values of the J distribution, 0.82 in CPF index 0 and 0.69–0.87 in CPF indices 2 to 4, indicate a large dispersion from one sample to another. IR values strongly decrease in ultramylonites (CPF index 5), and the distribution of J is positively skewed from CPF indices 1 to 5. Analyzed domains with less than 1000 grains (orange data in Figure 8a) are excluded from statistics because of the abnormally high J values calculated for them (Figure S1 in Supporting Information S1 and Table S3 in Supporting Information S2).

Median M values are low, below 0.07 overall; they slightly increase from CPF indices 1 to 4 and then decrease from CPF indices 4 to 5 (Figure 8b). The statistic distribution ranges (i.e., IR) are large, 0.06 in CPF

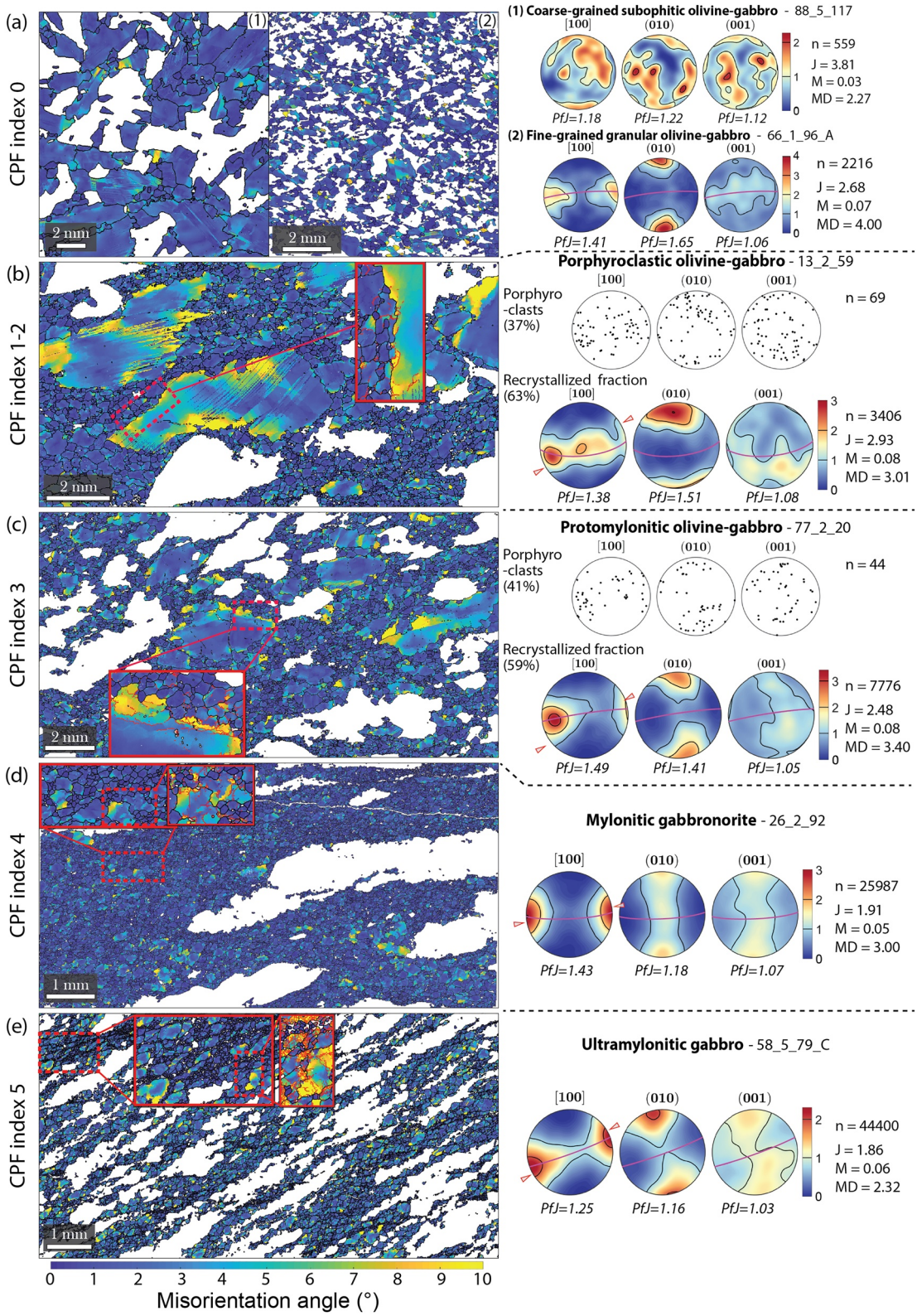
(a)
CPF index 0
(1)
(2)
2 mm
2 mm
(1) Coarse-grained subophitic olivine-gabbro - 88_5_117
[100] (010) (001)
PfJ=1.18 PfJ=1.22 PfJ=1.12
n = 559
J = 3.81
M = 0.03
MD = 2.27
(2) Fine-grained granular olivine-gabbro - 66_1_96_A
PfJ=1.41 PfJ=1.65 PfJ=1.06
n = 2216
J = 2.68
M = 0.07
MD = 4.00
(b)
CPF index 1-2
2 mm
Porphyroclastic olivine-gabbro - 13_2_59
Porphyro -clasts (37%)
n = 69
Recrystallized fraction (63%)
PfJ=1.38 PfJ=1.51 PfJ=1.08
n = 3406
J = 2.93
M = 0.08
MD = 3.01
(c)
CPF index 3
2 mm
Protomylonitic olivine-gabbro - 77_2_20
Porphyro -clasts (41%)
n = 44
Recrystallized fraction (59%)
PfJ=1.49 PfJ=1.41 PfJ=1.05
n = 7776
J = 2.48
M = 0.08
MD = 3.40
(d)
CPF index 4
1 mm
Mylonitic gabbronorite - 26_2_92
PfJ=1.43 PfJ=1.18 PfJ=1.07
n = 25987
J = 1.91
M = 0.05
MD = 3.00
(e)
CPF index 5
1 mm
Ultramylonitic gabbro - 58_5_79_C
PfJ=1.25 PfJ=1.16 PfJ=1.03
n = 44400
J = 1.86
M = 0.06
MD = 2.32
0 1 2 3 4 5 6 7 8 9 10
Misorientation angle (°)

Figure 6.

index 0 and 0.04 in CPF index 4 and they usually overlap from one CPF index to another. The data distribution is negatively skewed from CPF indices 1 to 3, and rather normal from 4 to 5.

The M index indicate higher CPO strength for fine-grained magmatic samples (CPF index 0, gray data points Figure 8b). The evolution of J and M indices with increasing CPF indices from 1 to 5 shows a bell-shaped distribution. The peak maximum of this distribution is at CPF indices 2–3 for J and 3–4 for M (taking into account the complete overlap of the neighboring distributions).

6.2. Misorientation Analysis

Deformation at high temperature induces storage of energy in strained grains that is released up by the creep of crystal defects toward the grain boundary and can arrange in subgrain structures. Produced by the dislocation motion through slip systems, they are characterized by a local rotation specific to the dislocations that they are made up of Amelinckx and Dekeyser (1959). These rotations and axes along which they arrange are indicative of the activated slip systems (e.g., Lloyd et al., 1997).

Intracrystalline misorientation analysis indicates dominant amounts of low angle correlated misorientations (<10°) within grains in 77 microstructural domains (e.g., Figure 6 and Figure S2 in Supporting Information S1). This is observed from CPF indices 0 to 5, and predominates in protomylonitic to ultramylonitic domains (CPF indices 3 to 5). In the 38 other microstructural domains, similar amounts of low and high angle misorientations (<10° and 150°–180°, respectively) are observed. Fifty nine domains indicate more than 20% of misorientations in the class 0°–10°, and 88 domains indicate more than 10% of misorientations in that class. This strongly suggests that the main active mechanism is SGR (e.g., Poirier & Guillopé, 1979). Displayed in inverse pole figure, the rotation axes of intracrystalline misorientations are always preferentially arranged around the [100] axis, sometimes with variations of up to 20° toward the north pole (Figure S2 in Supporting Information S1 and Figure 9a, top). Other misorientation axes are present at subgrain boundaries but are less common. The misorientation axis and the slip direction in slip systems are orthogonal, or at least at high angle for edge dislocations in plagioclase (e.g., Kruse et al., 2001). Then, by considering the [100](010) slip system inferred from pole figures (Figures 6 and 7), the misorientation axis displayed in inverse pole figure should be different from [100]. Consistently with the pole figures (Figures 6 and 7), misorientation rotation axes at grain boundaries are preferentially located around (010) (Figure S2 in Supporting Information S1 and Figure 9a, middle and bottom). Then as (010) is the plane parallel to the foliation in almost all analyzed domains, it is possible that subgrain boundaries, with a [100] misorientation axis, mainly consist of tilt boundaries, while grain boundaries, with a [010] misorientation axis, consist of twist boundaries.

The analysis of misorientations related to recrystallization was performed on 52 plagioclase porphyroclast-recrystallized mantle pairs in 33 microstructural domains of variably deformed textures (CPF indices 1 to 4), mainly porphyroclastic and protomylonitic (CPF indices 2 and 3). Rotation axes of misorientations at parent grains boundaries (Figure 9a, middle) correspond to a mix of those of misorientations at subgrain boundaries (Figure 9a, top) and at recrystallized grains boundaries, dominantly along the (010) plane (Figure 9a, bottom). At parent grains boundaries, ubiquitous high misorientations indicate a general scattering of the neighboring recrystallized grains (Figure 9b). Two groups of misorientations are distinguished: (a) with boundary segments of 10°–60° angles and (b) with 120°–180° angles (Figure 9b). Group 1 is found in 35 porphyroclast-recrystallized mantle pairs (over 52 analyzed) and combines with group 2 in 30 pairs. 17 pairs display a non-zero flat misorientation profile from ∼10° to 100°, increasing for higher misorientations (>120°). In these pairs, a major part of grain boundaries are twin boundaries (misorientations of 180°). The two types of profiles (one with groups 1 and 2, and the other with only the group 2) are also observed by looking at differences in orientations between parent grains and their second- and third-order neighbors.

Figure 6. Maps of misorientations from grain average orientation in plagioclase, and associated pole figures (average grain orientation data, lower hemisphere, equal-area projection) measured in representative domains from CPF indices 0 to 5. The trace of (010) in plagioclase (defined by the principal eigen-vector of the orientation tensor) is represented by the pink great circles, and the orientation of the trace of the foliation measured in samples, when observed with confidence, is indicated by the red arrows at the periphery of [100] pole figures. The white color in maps corresponds to other phases, and red limits in insets are subgrain boundaries. Contour intervals are multiples of a uniform distribution, and the minimum density is set to zero for comparison between analyzed domains. Maps and pole figures are presented respectively with the depth increasing from the top to the bottom and from north to south pole. "*n*" is the number of grains, "J" is the J index, "M" is the M index, "MD" is the maximum density, and "PfJ" are the pole densities of each pole figures (see text for explanations). Indicated percentages in (c and d) are area fractions of porphyroclasts and recrystallized grains.

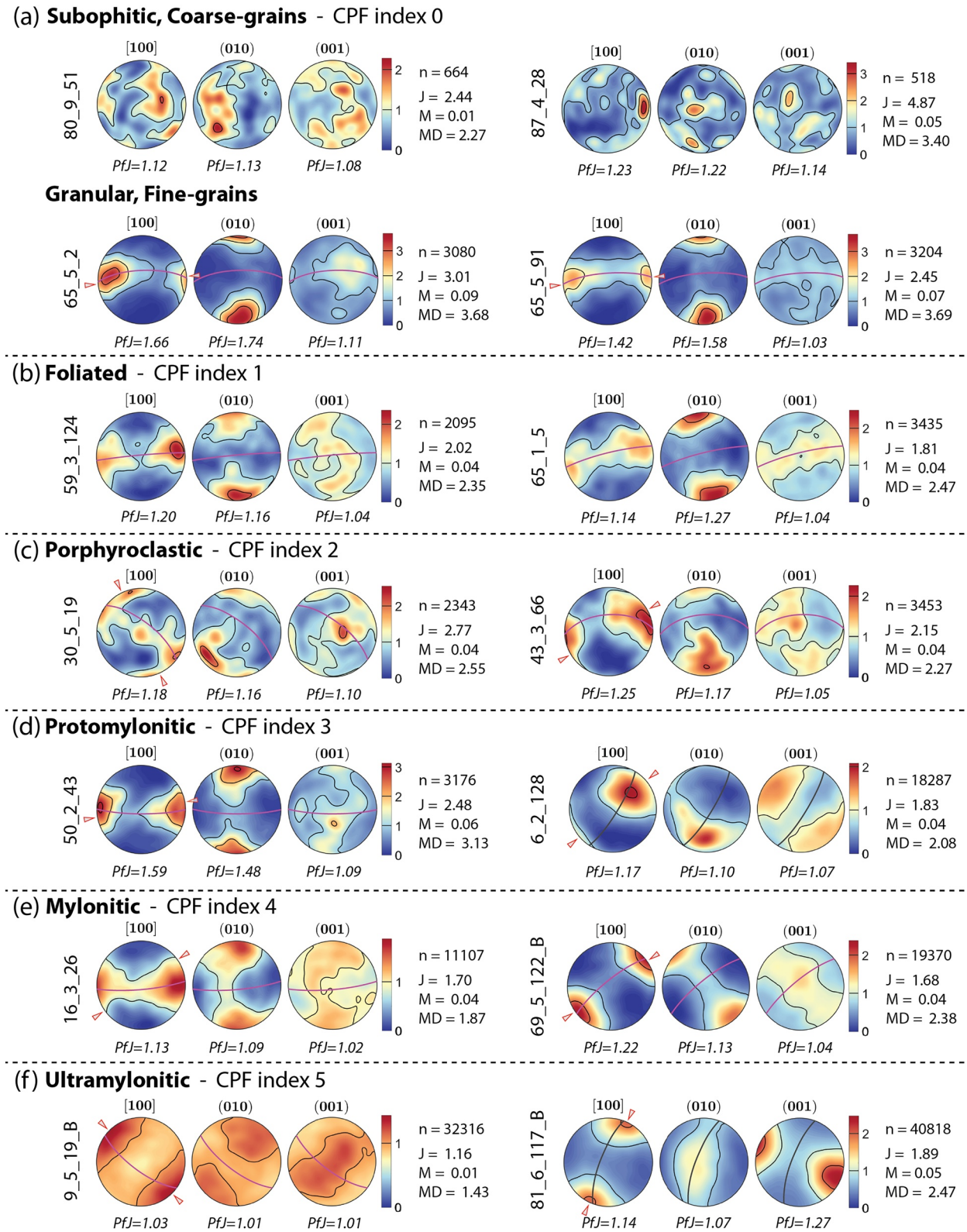
(a) Subophitic, Coarse-grains - CPF index 0
80_9_51
[100] (010) (001)
n = 664
J = 2.44
M = 0.01
MD = 2.27
PfJ=1.12 PfJ=1.13 PfJ=1.08
87_4_28
n = 518
J = 4.87
M = 0.05
MD = 3.40
PfJ=1.23 PfJ=1.22 PfJ=1.14
Granular, Fine-grains
65_5_2
n = 3080
J = 3.01
M = 0.09
MD = 3.68
PfJ=1.66 PfJ=1.74 PfJ=1.11
65_5_91
n = 3204
J = 2.45
M = 0.07
MD = 3.69
PfJ=1.42 PfJ=1.58 PfJ=1.03
(b) Foliated - CPF index 1
59_3_124
n = 2095
J = 2.02
M = 0.04
MD = 2.35
PfJ=1.20 PfJ=1.16 PfJ=1.04
65_1_5
n = 3435
J = 1.81
M = 0.04
MD = 2.47
PfJ=1.14 PfJ=1.27 PfJ=1.04
(c) Porphyroclastic - CPF index 2
30_5_19
n = 2343
J = 2.77
M = 0.04
MD = 2.55
PfJ=1.18 PfJ=1.16 PfJ=1.10
43_3_66
n = 3453
J = 2.15
M = 0.04
MD = 2.27
PfJ=1.25 PfJ=1.17 PfJ=1.05
(d) Protomylonitic - CPF index 3
50_2_43
n = 3176
J = 2.48
M = 0.06
MD = 3.13
PfJ=1.59 PfJ=1.48 PfJ=1.09
6_2_128
n = 18287
J = 1.83
M = 0.04
MD = 2.08
PfJ=1.17 PfJ=1.10 PfJ=1.07
(e) Mylonitic - CPF index 4
16_3_26
n = 11107
J = 1.70
M = 0.04
MD = 1.87
PfJ=1.13 PfJ=1.09 PfJ=1.02
69_5_122_B
n = 19370
J = 1.68
M = 0.04
MD = 2.38
PfJ=1.22 PfJ=1.13 PfJ=1.04
(f) Ultramylonitic - CPF index 5
9_5_19_B
n = 32316
J = 1.16
M = 0.01
MD = 1.43
PfJ=1.03 PfJ=1.01 PfJ=1.01
81_6_117_B
n = 40818
J = 1.89
M = 0.05
MD = 2.47
PfJ=1.14 PfJ=1.07 PfJ=1.27

Figure 7.

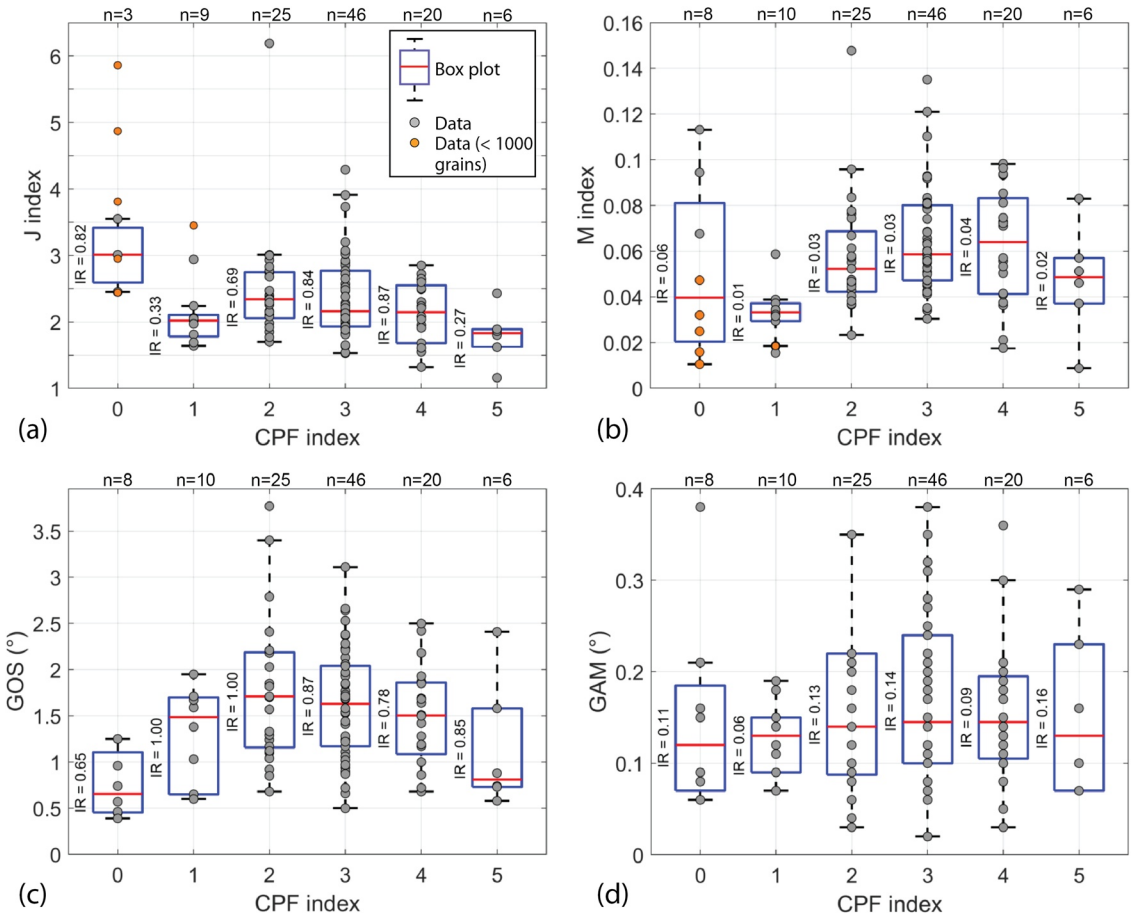

Figure 8. Fabric strength and misorientations indices of plagioclase grains. (a) J index and (b) M index evolution with CPF index in plagioclase. Note that orange data (<1000 grains) are excluded from J index statistics (see text). Box plot parameters, "IR" and "*n*" are detailed in the legend of Figure 4. (c) Average grain orientation spread (GOS) for plagioclase in the analyzed samples. It indicates the degree of torsion of the lattice at grain scale. (d) Mean of grain average misorientations (GAM) of plagioclase in the analyzed samples. It indicates the degree of local misorientations in grains. Average grain orientation data are used in these graphics and both porphyroclasts and recrystallized grains are considered.

However, when present group 1 is usually wider and shifted toward higher misorientations (40°–90°). No correlation was found between parent grains crystallographic orientations and the dispersion of crystallographic orientations of neighboring recrystallized grains. Other correlations with the textural position of parent grains (within the recrystallized matrix of plagioclase, or on contact with other phases) or the size of recrystallized grains have not been observed either.

Plagioclase grain deformation increases with increasing recrystallization in analyzed domains. GOS median values display a positively skewed distribution from CPF indices 0 to 5, with values ranging from ~0.65° to ~1.7°. The statistic distribution is characterized by an important dispersion with IR values ranging from 0.65° to 1.00°, and overlapping between CPF indices (Figure 8c and Table S3 in Supporting Information S2). A decrease of GOS values is observed in grains from ultramylonites (CPF index 5), where the median grain size is significantly reduced (21 μm; Table S3 in Supporting Information S2). Although median GAM values show a weak linear increase toward CPF index 4, the overlap between all IR does not permit to establish a clear tendency (Figure 8d and Table S3 in Supporting Information S2). Median GAM values are low and

Figure 7. Pole figures of plagioclase (average grain orientation data, lower hemisphere, equal-area projection) measured in representative domains in gabbros from CPF indices 0 to 5. The trace of the (010) plane in plagioclase is represented by the pink great circles, the trace of the (001) by the black great circles in (d and f), and the orientation of the trace of the foliation measured in thin section, when observed with confidence, is indicated by the red arrows at the periphery of [100] pole figures. The minimum density in pole figures is set to zero for direct comparison between analyzed domains. The parameters are the same as in Figure 6.

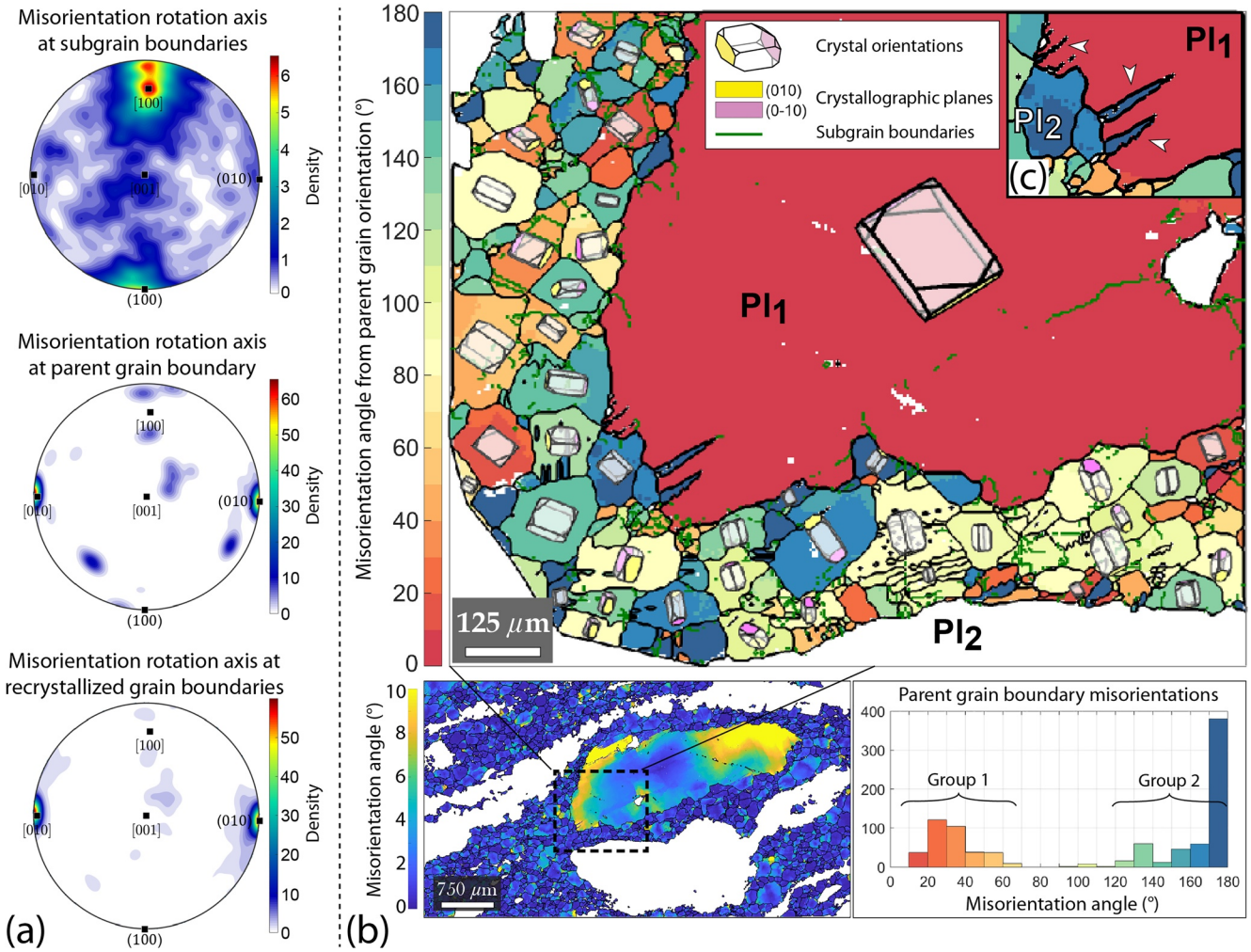

Figure 9. Representative porphyroclast-recrystallized mantle pair misorientation relations in plagioclase, microstructural domain 69_5_17 (CPF index 3). (a) IPF (antipodal, equal angle projection) of misorientation rotation axes at subgrain boundaries (top), parent grain boundary (middle), and recrystallized grain boundaries (bottom). (b) Misorientations between the plagioclase parent porphyroclast (red; Pl_1) and the recrystallized grains (red, green to blue colors; Pl_2), superimposed by oriented crystal shapes and subgrain boundaries (green limits). The bottom left misorientation map from grain average orientation in plagioclase indicates the analyzed region. The histogram shows parent grain boundary misorientations from its mean orientation. (c) Close-up showing tapered twins (white arrows) at the periphery of the parent grain (Pl_1).

ranges from 0.12° to ~0.14° with large IR values ranging from 0.06° to 0.16°. Again, the overlap between the statistic distributions is important (Figure 8d). A peculiar observation is that the GAM values are systematically higher in recrystallized grains than in magmatic porphyroclasts (Figure S3 in Supporting Information S1). This is explained by the localized nature of intragranular misorientations in grains, leading to higher measured misorientation density (hence a higher GAM) in newly and small recrystallized grains than in old and larger porphyroclasts.

7. Discussion

7.1. Lithologies and Deformation Intensity

As already reported by Miranda and John (2010) in dive samples from the surface of the Atlantis Bank, no differences in terms of deformation intensity (CPF indices) are observed between the sampled oxide-free and oxide-bearing lithologies. In addition to this observation, the increase in deformation intensity occurs with limited mineral modal changes (Figure 4a and Table S3 in Supporting Information S2), generalizing

these authors' conclusion to gabbroic lithologies in general that the primary rock composition has no influence on strain localization.

7.2. Crystallographic Preferred Orientations and Deformation Mechanisms of Plagioclase

Fine-grained granular domains (CPF index 0, Figure 7a) display CPO with a [100](010) fabric, interpreted as resulting from magmatic flow (e.g., Benn & Allard, 1989; Ji et al., 2014; Satsukawa et al., 2013). Although coarse-grained subophitic domains shown herein display no clear CPO (CPF index 0; e.g., Figures 6a and 7a), it is documented in coarse-grained olivine gabbros from Hole U1473A by Boulanger et al. (2021). The onset of plastic deformation in sampled domains (CPF indices 1 to 5) also results in the development of a [100](010) CPO (Figures 6b–6e and 7b–7f) with a common "host-controlled" relation between porphyroclasts and recrystallized grains (Figures 6b and 6c). The presence of a CPO in porphyroclasts from deformed domains could then result from the direct deformation of porphyroclasts leading to their reorientation; or from the preferential localization of deformation in intervals with a preexisting magmatic fabric. This magmatic fabric would define a "soft" orientation of crystals (Burg et al., 1986; Schmid, 1994) favoring the activity of the [100](010) slip system, or more generally [*hkl*](010). Note that a few analyzed domains (CPF indices 2 to 5) indicates CPO patterns consistent with the [100](001) slip system (Figures 7d and 7f, and possibly Figure 6d). Similar CPO have already been reported in the SWIR mylonites (Mehl & Hirth, 2008) and other OCC (e.g., Hansen et al., 2013; Harigane et al., 2008).

Overall, the intensity of plagioclase CPO is weak (Figures 8a and 8b). Similar fabric strength in gabbros mylonites are reported by Miranda et al. (2016) at the footwall of the Atlantis Bank, and by Mehl and Hirth (2008) in Hole 735B, who also measured higher strength in plagioclase monophase layers. The calculated CPO strength in plagioclase aggregates is weak in gabbroic rocks in general, except in some magmatic foliated gabbros (e.g., Satsukawa et al., 2013). CPO in deformed rocks, even when weak, is often interpreted as resulting from dislocation creep (e.g., Mehl & Hirth, 2008; Urai et al., 1986). Dynamic recrystallization processes via dislocation creep occurs within grain aggregates of the same type, at interphase boundaries (e.g., Poirier, 1985). Texturally, the general tendency of monomineralic banding arrangement forming a strain-induced foliation plane in samples from Hole U1473A could be consistent with a deformation dominated by dislocation creep (Figure 3) and enhances strain localization (e.g., Kenkmann & Dresen, 2002). Consistently, the increase of J index values from CPF indices 1 to 2, and of M index from CPF indices 1 to 4 are indicative of the building of a CPO, highlighting that the deformation occur in the dislocation creep regime (Figures 8a and 8b). The limited number of grains in coarse-grained undeformed domains (CPF index 0) does not allow to be conclusive about the evolution of the fabric strength from CPF indices 0 to 1 concerning the J index. However, the M index, which is not dependent of the number of analyzed grains by contrast to the J index (Skemer et al., 2005), seems to display an increase of the fabric strength from CPF indices 0 to 4 (for CPF index 0 the comparison is made with coarse-grained domains as they most probably corresponds to the protoliths of the deformed domains, see orange data in Figure 8b).

At hyper-solidus conditions, olivine crystals are the first to undergo plastic deformation (Yoshinobu & Hirth, 2002), and in hot geothermal lower crustal sections plagioclase is usually weaker than olivine and clinopyroxene (e.g., Homburg et al., 2010; Kronenberg & Shelton, 1980). The studied microstructures are consistent with these observations, and indicate that because of its important proportion (~60%), plagioclase accommodates alone most of rock's deformation (e.g., Ji et al., 2000). The evolution of the fabric strength presented in Figures 8a and 8b show a decrease in ultramylonites. This decrease is possibly an effect of the progressive SGR recrystallization, first occurring in porphyroclasts and continuing within the recrystallized grains as indicated by the important proportions of subgrain boundaries observed in recrystallized grains of mylonites and ultramylonites (e.g., Figures 6d and 6e). This effect of the progressive recrystallization can combine with the change in the dominant active slip system at decreasing deformation temperatures to produce the observed fabric strength decrease. Other mechanisms than dislocation creep could also account for this fabric strength decrease, such as the heterogeneous nucleation of amphibole grains (up to ~14% in ultramylonites) or the activation of diffusion creep thanks to hydrothermal fluid circulation (e.g., Mehl & Hirth, 2008; Nozaka et al., 2019). In addition, the reduced grain size in ultramylonites (median = 21 μm) and the likely decrease in deformation temperature in the presence of hydrothermal fluids, which must induce significant chemical potential gradients, could favor the activity of grain-size-sensitive processes such as

granular flow (e.g., Mehl & Hirth, 2008; Oliot et al., 2010, 2014; Paterson, 1995; Stünitz & Fitz Gerald, 1993). Granular flow is likely to have occurred in the microstructural domain 9_5_19_B, corresponding to a plagioclase-amphibole bearing narrow ultramylonite, displaying a very weak CPO (Figure 7f). Kenkmann and Dresen (2002) proposed that in fine-grained mafic mylonites, fluid-assisted diffusion and dislocation creep are activated together to accommodate grain-boundary sliding. Chemical potentials are also known to enhance diffusion processes such as CIGM, which is a strain softening process (Hay & Evans, 1987; Hirth & Tullis, 1992; Urai et al., 1986). Other studies in gabbros deformed in OCC systems also proposed the activation of grain-size-sensitive processes such as grain boundary sliding to explain the observation of weak CPO in highly deformed samples (e.g., Harigane et al., 2008; Mehl & Hirth, 2008; Miranda et al., 2016).

Seven of the 115 microstructural domains with a foliation parallel to (001) in plagioclase rather than the common (010) are characterized by high amphibole contents (11%–28%), and by a high oxide content (ilmenite: 11%, and magnetite: 10%) in another domain. The median recrystallized grain size in all these studied domains is ∼30 μm. In mylonites and ultramylonites from the Godzilla Megamullion (Parece Vela Basin, Philippine Sea), Harigane et al. (2011) proposed a transition from dislocation creep to grain-size-sensitive creep with decreasing temperature to explain the change from [100](010) to [100](001) slip systems in CPO patterns. For the same reasons as in ultramylonites, a transition to a grain-size-sensitive creep such as granular flow could explain the transition from a CPO pattern to another. However, an alternative explanation that does not require a change in deformation mechanism, also linked to deformation temperature, is that the dominant active slip system changed. As shown in Figure 1, the activity of the [100](010) slip system is documented over a large range of high temperatures (∼600°–900°C), and a decreasing temperature (<750°C) during deformation could favor the activity of other slip systems, here [100](001), at the expense of the former one. Then, these domains could correspond to intervals deformed during the later solid state–semi-brittle deformation episode at 665 ± 40°C (Miranda & John, 2010). This hypothesis is better consistent than a switch in CPO patterns arising from a change in deformation mechanism, with the majority of ultramylonites displaying clear CPO patterns indicating [100](010) slip, although granular flow may also have occurred.

7.3. Dynamic Recrystallization Processes of Plagioclase

In deformed domains (CPF indices 2 to 5), core-mantle structures develop because of extensive recrystallization of the main phases (e.g., Figures 3c, 3d and 5d–5f). Subgrain boundaries in plagioclase porphyroclasts (Figures 5d and 7b–7e) are associated with dominant frequencies of low-angle misorientations (<10°), representing 20% of all misorientations in 59 analyzed domains and 10% in 88 domains (Figure S2 in Supporting Information S1). A host-controlled relationship between magmatic parent and recrystallized grains is inferred from the CPO of most domains (e.g., Figures 7b and 7c). Finally, the ubiquitous presence of recrystallized grains with 20°–60° of misorientation from the parent grain (group 1, Figure 9b) is consistent with a progressive rotation of the newly formed grains to the parent grain. All these observations argue in favor of SGR as the main recrystallization mechanism in plagioclase. This recrystallization process in plagioclase grains is commonly described in Atlantis Bank mylonites (Gardner et al., 2020; Mehl & Hirth, 2008; Miranda et al., 2016; Miranda & John, 2010; Taufner et al., 2021).

Important fractions of high misorientations can be found at the direct contact between parent and recrystallized grains (group 2, 100°–180°). This might indicate that recrystallization initiated within microcracks (e.g., Escher & Gottstein, 1998; Kruse et al., 2001; Okudaira et al., 2017), or by SGR from a twinned domain of the parent grain. In the later, the misorientation between the twinned domains would be 180° (e.g., Figure 9c). Then, grains achieving a rotation of 60° from a twinned domain (reference orientation at 180°) would be measured with a misorientation of 120° with respect to the parent grain orientation (reference orientation at 0°). This could be consistent with the widespread observation of tapered twins in plagioclase grains (e.g., Figure 5a, 5b, 5d and 9c). Concerning microfracturing, this produces nuclei that rapidly grow by grain boundary migration, resulting in arbitrary misorientations from their parent grain. However, the limitation of this hypothesis in our samples resides in the widespread observation of a crystallographic control on the formation of recrystallized grains (Figure 9a), best consistent with the formation of new grains by progressive SGR (Lloyd et al., 1997). In addition, grains with a high angle misorientation to the parent grain (group 2, Figure 9b) are heterogeneously distributed. One would expect these grains to be aligned if

nucleation occurred along microcracks. However, it is a possible mechanism for the very first stages of shear-band development in 4 porphyroclastic to protomylonitic domains (CPF indices 2 and 3, microstructural domains 34_2_98, 44_1_105_B, 67_1_73 and 67_7_110_A, Figure S4 in Supporting Information S1 and Table S3 in Supporting Information S2), where thin and straight recrystallized bands (100–150 μm large) are found within large porphyroclasts (450–500 μm).

In a context of continuous deformation from hyper-solidus to lower grade metamorphic conditions (granulite to amphibolite), one may expect that recrystallized grains continued to deform after they detached from their parent grain. This is observed in analyzed domains with an increasing development of subgrain boundaries from porphyroclastic to ultramylonitic textures (CPF indices 2 to 5, Figure 6b–6e), and by the general observation of higher GAM values in recrystallized grains than in porphyroclasts (Figure S3 in Supporting Information S1). It indicates an intracrystalline hardening of grains as recrystallization progresses, together with a general grain size reduction. This strain hardening arising during dislocation creep could then favor the activation of other deformation mechanisms such as grain-size-sensitive process and chemical diffusion (i.e., granular flow).

In 38 microstructural domains (mostly CPF indices 0 to 2), plagioclase grain boundaries are lobate and the recrystallized grain size is higher than in samples showing evidence of dominant SGR (120–300 μm, e.g., Figure 5a). Also, the fraction of low angle misorientations (>10°) is small compared to higher misorientations, attesting for GBM.

The dominant recrystallization mechanism varies with the extent of deformation, but also varies with depth (Figure 10a). SGR is ubiquitous throughout the hole whereas GBM is dominant at CPF indices 1 and 2 in the lower parts of the hole (~500–800 mbsf). In this lower interval, SGR is dominantly observed in zones of more intense and localized deformation (CPF indices >3; Figures 10a and 10b) as already observed in granulitic submersible mylonite samples by Miranda and John (2010). The recrystallized grain size associated with SGR in localized zones from this lower interval is on average 49 μm (±25 μm), about 20 μm smaller than for the upper interval, where it is of 72 μm (±28 μm) (Figures 10b and 10c), and third time smaller than for GBM recrystallized grains (on average 167 μm ± 88 μm). This is consistent with the fact that areas of reduced grain size by dynamic recrystallization, here SGR, associated with a CPO (acting as a local geometrical softening) are known to induce softening, enhancing strain localization (Ji & Mainprice, 1990; Tullis & Yund, 1985; Urai et al., 1986).

Together with the common observation of undulose extinction in grains from undeformed microstructural domains (Figure 6a), this suggests that plastic deformation started early, during post-magmatic stages (Dick, MacLeod, et al., 2019). The range of activity of GBM and SGR in plagioclase is rather similar at high temperatures (>600°C, Figure 1), so differences in the temperature of deformation between the upper and lower parts of the hole cannot explain the change in recrystallization mechanisms. Variations in strain are likely to account for the transition between GBM (lower strain and/or strain rate) and SGR (higher strain and/or strain rate). Differential stress calculations performed in recrystallized plagioclase grains support this hypothesis, as previously described in Mehl and Hirth (2008), using the Twiss (1977) equation for recrystallized grain size paleopiezometer. For recrystallized grains resulting from GBM (average grain size of ~167 μm) this calculation gives differential stresses of ~32 MPa, while for recrystallized grains resulting from SGR (average grain size of ~65 μm) the calculation yield a paleostress of ~61 MPa. Furthermore, the average recrystallized grain sizes associated with SGR vary between the upper part (~72 μm) and lower part (~49 μm) of the hole (Figures 9b and 9c). Thus, the more pervasive ductile deformation in the upper interval indicates lower differential stresses (~57 MPa above 500 mbsf) than in the lower interval (~74 MPa below 500 mbsf) where deformation is mostly localized.

The rare occurrence of BLG in plagioclase is mainly documented in domains from the upper 200 m of Hole U1473A, and a different temperature of deformation is likely as BLG is documented *ad maximam* at ~700°C while SGR occurs at least up to ~900°C in naturally deformed plagioclase aggregates (Figure 1). This could suggest that the lowest temperature deformation event (<700°C; Miranda & John, 2010) is important in the upper 200 m of the hole. The widespread crystal plastic deformation in the upper 500–600 mbsf of Hole U1473A is interpreted to result from the activity of the detachment fault that exhumed the gabbroic pluton forming nowadays the Atlantis Bank (MacLeod et al., 2017).

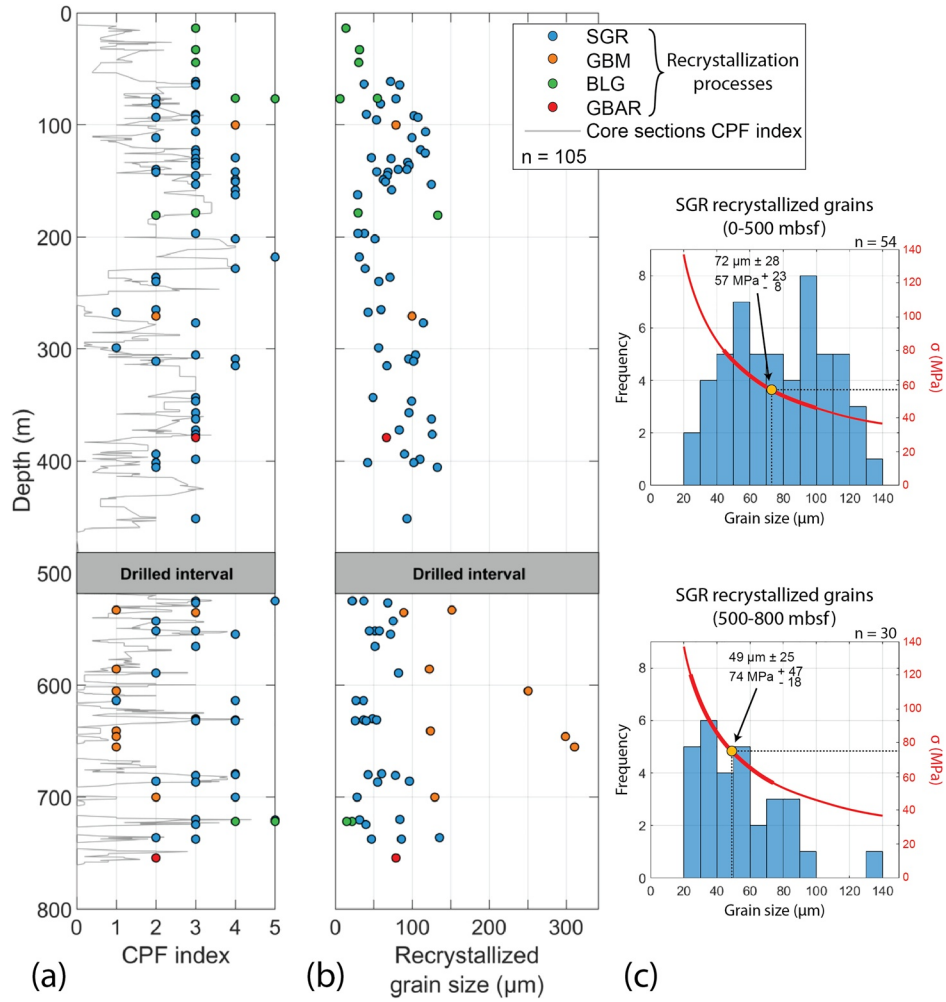

Figure 10. Recrystallization processes and associated grain sizes in plagioclase grains. (a) Dominant recrystallization processes in plagioclase as a function their CPF index along depth in Hole U1473A. The gray line corresponds to the CPF index of core sections (see Figure 2c). (b) Recrystallized grain size and associated recrystallization processes along depth. Recrystallization processes: SGR: subgrain rotation; GBM: grain boundary migration; BLG: bulging; GBAR: grain boundary area reduction (i.e., static recrystallization). (c) Histograms of recrystallized grain sizes associated with SGR recrystallization. The red curve corresponds to associated differential stresses calculated with Twiss (1977) equation for recrystallized grain size paleopiezometer. The geometric mean grain size and the associated paleostress are represented by the orange dots. The bold part of the red curve corresponds to paleostresses related to the standard deviation around the mean grain size. "*n*" is the number of analyzed microstructural domains.

7.4. Slip Systems Activity During Crystal-Plastic Deformation

A majority of microstructural domains display a foliation subparallel to the preferred orientation of plagioclase (010), associated with a lineation on [100] (Figures 6 and 7). This suggests the activity of the [100](010) slip system during crystal-plastic deformation. The analysis of misorientation rotation axes at subgrain boundaries in plagioclase indicates a strong maximum at or near [100] in all microstructural domains (e.g., Figure 9a). Previous studies of slip systems in plagioclase indicate that [100] is the misorientation rotation axis associated with the edge segments of [001](010) dislocation system (e.g., Kruse et al., 2001; Svahnberg & Piazolo, 2010). Similar observations are documented in mylonites of the Kane OCC (Mid-Atlantic ridge, e.g., Hansen et al., 2013). However, pole figures of a majority of analyzed domains are characterized by the preferred orientation of (010) for the foliation and [100] for the lineation, consistent with the activity of the [100](010) slip system. The ubiquitous [100] misorientation axis on subgrain boundaries must indicate the activity of the [001](010) slip system that does not reflect in the CPO. The observation of different slip

systems at subgrain boundaries than the one inferred from CPO was also reported by Mehl and Hirth (2008) and Svahnberg and Piazolo (2010) in plagioclase. Mehl and Hirth (2008) proposed that porphyroclasts subgrain boundaries are not dominantly composed of the easiest slip systems, or that the critical resolved shear stress of slip systems is not the only parameter to control the development of the CPO. The general observation of an "host-controlled" relation between porphyroclasts and recrystallized grains, the presence of a CPO with a similar slip plane in igneous textures (CPF index 0) and in deformed samples (CPF indices 1 to 5, Figure 6), and the parallelism between this slip plane and the foliation suggest a general "soft" orientation of porphyroclasts in studied domains. This supports the activity of slip systems different from the easiest one in porphyroclasts, with [001](010) dominantly observed at subgrain boundaries, while the dominant slip system producing the CPO is [100](010).

Further analyses of misorientations aiming at the active slip systems identification in plagioclase grains are conducted through the selection of grains with, respectively, their (010) and (001) planes parallel to the analyzed plane (see Section 4.3 in Methods). In the first group (i.e., (001) parallel to the plane of analysis), 79 microstructural domains show a clustering of misorientation axes around [101] dominantly, and [001] (Figure 11a). In many domains the maximum is centered on [101] but extends toward [001], and can form a semi-girdle between the [001] and [201] directions (aligned in (010)). [101] is nearly orthogonal to (001), thus misorientations result from the motion of screw dislocations. Direct identification of the Burgers vector of the corresponding dislocations system is not straightforward as any direction orthogonal to the misorientation axis is possible (Lloyd et al., 1997). As explained in Section 4.3 the closest directions to the lineation are considered the better candidates for glide. The possible slip directions comprised in (001) are: [100], ½[110], and ½[1$\bar{1}$0] (e.g., Kruse et al., 2001; Marshall & McLaren, 1977). Deformation in Hole U1473A mainly occurs as reverse shearing, so the lineation (here parallel to [100] of plagioclase) should be close to the shear direction. Then, the three slip directions are likely by considering that ½[110] and ½[1$\bar{1}$0] could be activated simultaneously. A second maximum is found in 31 domains, usually associated with the previous one, clustering around [100] (Figure 11a). This maximum lies in the (001) plane, and can thus be related to edge dislocations. Possible slip directions are: ½[110] and ½[1$\bar{1}$0], and it is proposed that both slip systems were active for the same reason as for the [101] misorientation axis.

The second group of grains (i.e., (010) parallel to the plane of analysis) shows a maximum of misorientation axes on [100] (93 microstructural domains, Figure 11b). This direction is within the (010) plane, sub-parallel to the foliation, and results from the activity of the [001](010) slip system. A sub-maximum is found around the [010] direction (38 microstructural domains). In that case, misorientations are orthogonal to the slip plane (010) and correspond to screw dislocations. The possible slip directions are: [100], [001], [201], and

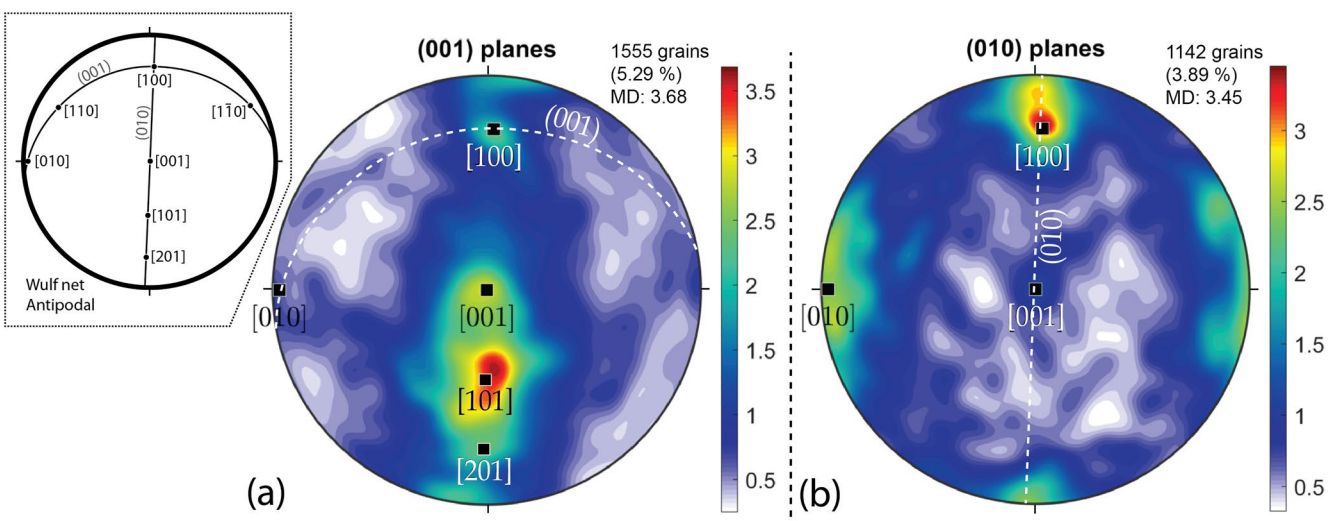

Figure 11. Typical IPF (antipodal, equal angle projection) showing misorientation rotation axes at subgrain boundaries in grains with (a) their (001) plane and (b) their (010) plane parallel to the plane of analysis (microstructural domain 69_5_17). The corresponding percentage of grains in the domain is indicated, MD is the maximum density. The top left inset indicates the location of the discussed crystallographic directions and planes (modified after Kruse et al., 2001).

[101] (e.g., Kruse et al., 2001; Marshall & McLaren, 1977). The directions [201] and [100] are the most likely due to their geometrical relationship to the lineation in the studied domains (parallel to [100]), whereas [101] and [001] are at high angle from the [100] direction. In addition, the [100] slip direction corresponds to the [100](010) slip system that produced the CPO. However, the [101] and [001] directions cannot be completely ruled out only based on their high angle to the lineation.

In summary, the dominant active slip systems identified with misorientations are: [100](001), ½[110](001), ½[1 $\bar{1}$0](001), and [001](010); and other possible slip systems of secondary importance are: [100](010) or [201](010), or less likely [001](010) or [101](010).

The slip systems identified both in porphyroclasts and recrystallized grains are indicative of different temperature ranges for active crystal plasticity. The most common slip systems in the sample suite is [100](010). It is documented over a wide range of temperatures, and corresponds to the slip system dominantly observed at the highest temperatures (~900°C, Figure 1). Documented as dominant from 600°C to 800°C, [001](010) is the main slip system active at subgrains (Figure 1). Both may have operated simultaneously in plagioclase grains from the onset of crystal plasticity during the first episode of solid state deformation from ~1000° to ~860°C, leading to the observed CPO and dominant subgrain boundaries development (Gardner et al., 2020; Mehl & Hirth, 2008; Miranda & John, 2010). The two other important slip systems identified at subgrain boundaries are ½[110](001) and ½[1 $\bar{1}$0](001). Their range of activity is documented for lower temperatures than the two others: mainly ~600° to 700°–750°C for ½[110](001), and mainly <600°–700°C for ½[1 $\bar{1}$0](001) (Figure 1). Finally, the [100](001) slip system observed in CPO patterns of a few microstructural domains is mainly active from ~600° to 750°C and documented up to ~900°C (Figure 1). The rising activity of these three slip systems gliding in (001) could possibly be related to the latest episode of mylonitization <700°C (Miranda & John, 2010) as their presence seems limited and confined at subgrain boundaries (except for [100](001), see Section 7.2).

8. Conclusion

Crystal-plastic deformation of plagioclase is common in the gabbroic lithologies of IODP Hole U1473A, and results in foliated to ultramylonitic textures. The sampled lithologies indicate a progressive monomineralic banding arrangement as plagioclase dynamic recrystallization increases until it is complete in ultramylonites, together with a general decrease of the recrystallized grain size. Plastic deformation in these rocks is dominated by dislocation creep, which reflects in plagioclase by the development of a CPO produced by the [100](010) slip system, and locally by [100](001). This second CPO produced by the [100](001) slip system is interpreted to arise from lower temperature of deformations (<700°C) rather than a change in deformation mechanism. The intensity of the CPO is weaker in ultramylonites as indicated by lower J and M indices values. This decrease in intensity is interpreted to possibly arise from the scattering of grain orientation during recrystallization and a change in slip system activity during lower temperature deformations. For a fraction of the analyzed domains, a change in the main active deformation mechanism made feasible by reduced grain size and hydrothermal fluid circulation is likely. Diffusion and grain-size-sensitive processes, in combination or individually, would then have produced a randomization of the CPO.

Recrystallization in plagioclase grains results from progressive subgrain rotation as evidenced by (a) the orientation relationship between magmatic parent grains and their neighboring recrystallized mantles, (b) the widespread observation of subgrain boundaries and intracrystalline misorientations (<10°), and (c) the crystallographic control on recrystallized grains boundaries. SGR is dominant throughout Hole U1473A, although in the lowermost 300 m it is more associated to areas of localized deformations when GBM prevails away from these localized shear zones. SGR in these localized domains produce smaller recrystallized grains than in the upper part of the hole where the deformation is pervasive. This results in higher estimated differential stresses in the lower part of Hole U1473A, ~20 MPa above the value calculated for the upper part.

The detailed analysis of misorientations within plagioclase grains reveals the activity of four dominant slip systems in addition to [100](010) that produced the CPO: [001](010), [100](001), ½[110](001), and ½[1 $\bar{1}$0](001). The activity of the two main slip systems, [100](010) and [001](010), is most probably related to an episode of solid state deformation at high temperatures (860°–1000°C). By contrast, the three other could

correspond to the episode of moderate deformation temperatures (650°–700°C) in the semi-brittle ductile regime, possibly occurring later during the exhumation history of the Atlantis Bank.

Data Availability Statement

The data set is accessible in the PANGEAE data repository (https://doi.org/10.1594/PANGAEA.932302).

Acknowledgments
This research used samples and data provided by the International Ocean Discovery Program. The authors thank the members of the IODP Expedition 360 Science Party, the captain and crew of the JOIDES Resolution, and the staff at the Kochi Core Center. The authors thank C. Nevado and D. Delmas for careful thin section preparation. E. Schettino is acknowledged for EBSD measurements during his internship in Montpellier, and M. Boulanger for the access to EBSD data in three fine-grained olivine gabbro samples. The authors thank R. Hielscher, R. Kilian, and A. Tommasi for their help with MTEX. H. Stünitz, A. Tommasi, and D. Mainprice are acknowledged for fruitful discussions. The authors are also grateful for the substantial improvements provided by two anonymous reviewers and the editor S. Parman. This study was funded by IODP-France.

References

Amelinckx, S., & Dekeyser, W. (1959). The structure and properties of grain boundaries. In Seitz, F., & Turnbull, D. (Eds.), *Solid state physics* (Vol. 8, pp. 325–499). Elsevier. https://doi.org/10.1016/S0081-1947(08)60482-8

Bailey, J. E., & Hirsch, P. B. (1962). The recrystallization process in some polycrystalline metals. *Proceedings of the Royal Society of London—Series A: Mathematical and Physical Sciences*, *267*(1328), 11–30. https://doi.org/10.1098/rspa.1962.0080

Baines, A. G., Cheadle, M. J., Dick, H. J. B., Scheirer, A. H., John, B. E., Kusznir, N. J., & Matsumoto, T. (2003). Mechanism for generating the anomalous uplift of oceanic core complexes: Atlantis Bank, Southwest Indian Ridge. *Geology*, *31*(12), 1105. https://doi.org/10.1130/G19829.1

Bell, T. H., & Johnson, S. E. (1989). The role of deformation partitioning in the deformation and recrystallization of plagioclase and K-feldspar in the Woodroffe Thrust mylonite zone, central Australia. *Journal of Metamorphic Geology*, *7*(2), 151–168. https://doi.org/10.1111/j.1525-1314.1989.tb00582.x

Benn, K., & Allard, B. (1989). Preferred mineral orientations related to magmatic flow in ophiolite layered gabbros. *Journal of Petrology*, *30*(4), 925–946. https://doi.org/10.1093/petrology/30.4.925

Blum, P., Dick, H. J., MacLeod, C. J., & Expedition 360 Scientists. (2017). *Hole U1473A remediation operations, Expedition 362T*. International Ocean Discovery Program. https://doi.org/10.14379/iodp.proc.360.2017

Boulanger, M., France, L., Ferrando, C., Ildefonse, B., Ghosh, B., Sanfilippo, A., et al. (2021). Magma-Mush Interactions in the Lower Oceanic Crust: Insights From Atlantis Bank Layered Series (Southwest Indian Ridge). *Journal of Geophysical Research: Solid Earth*, *126*(9). https://doi.org/10.1029/2021jb022331

Brewer, L. N., Field, D. P., & Merriman, C. C. (2009). Mapping and assessing plastic deformation using EBSD. In Schwartz, A. J., Kumar, M., Adams, B. L., & Field, D. P. (Eds.), *Electron backscatter diffraction in materials science* (pp. 251–262). Boston, MA: Springer US. https://doi.org/10.1007/978-0-387-88136-2_18

Bunge, H. J. (1982). *Texture analysis in materials science: Mathematical methods*. Butterworth. https://doi.org/10.1016/C2013-0-11769-2

Burg, J. P., Wilson, C. J. L., & Mitchell, J. C. (1986). Dynamic recrystallization and fabric development during the simple shear deformation of ice. *Journal of Structural Geology*, *8*(8), 857–870. https://doi.org/10.1016/0191-8141(86)90031-3

Cannat, M. (1993). Emplacement of mantle rocks in the seafloor at mid-ocean ridges. *Journal of Geophysical Research: Solid Earth*, *98*(B3), 4163–4172. https://doi.org/10.1029/92JB02221

Debat, P., Soula, J.-C., Kubin, L., & Vidal, J.-L. (1978). Optical studies of natural deformation microstructures in feldspars (gneiss and pegrnatites from Occitania, southern France). *Lithos*, *11*(2), 133–145. https://doi.org/10.1016/0024-4937(78)90004-x

Dell'Angelo, L. N., & Tullis, J. (1996). Textural and mechanical evolution with progressive strain in experimentally deformed aplite. *Tectonophysics*, *256*(1–4), 57–82. https://doi.org/10.1016/0040-1951(95)00166-2

Dick, H. J. B., Blum, P., MacLeod, C. J., & Expedition 360 Scientists. (2017). *Expedition 360 summary*. International Ocean Discovery Program. https://doi.org/10.14379/iodp.proc.360.2017

Dick, H. J. B., Kvassnes, A. J. S., Robinson, P. T., MacLeod, C. J., & Kinoshita, H. (2019). The Atlantis Bank Gabbro Massif, Southwest Indian Ridge. *Progress in Earth and Planetary Science*, *6*(1), 64. https://doi.org/10.1186/s40645-019-0307-9

Dick, H. J. B., MacLeod, C. J., Blum, P., Abe, N., Blackman, D. K., Bowles, J. A., et al. (2019). Dynamic accretion beneath a slow-spreading ridge segment: IODP Hole 1473A and the Atlantis Bank oceanic core complex. *Journal of Geophysical Research*, *124*(12), 12631–12659. https://doi.org/10.1029/2018JB016858

Dick, H. J. B., Meyer, P. S., Bloomer, S., Kirby, S., Stakes, D., & Mawer, C. (1991). *Proceedings of the Ocean Drilling Program, 118 Scientific Results* (Vol. 118). Ocean Drilling Program. https://doi.org/10.2973/odp.proc.sr.118.1991

Dick, H. J. B., Natland, J. H., Alt, J. C., Bach, W., Bideau, D., Gee, J. S., et al. (2000). A long in situ section of the lower ocean crust: Results of ODP Leg 176 drilling at the Southwest Indian Ridge. *Earth and Planetary Science Letters*, *179*(1), 31–51. https://doi.org/10.1016/S0012-821X(00)00102-3

Drury, M. R., & Urai, J. L. (1990). Deformation-related recrystallization processes. *Tectonophysics*, *172*(3–4), 235–253. https://doi.org/10.1016/0040-1951(90)90033-5

Escartín, J., & Canales, J. P. (2011). Detachments in oceanic lithosphere: Deformation, magmatism, fluid flow, and ecosystems. *Eos, Transactions American Geophysical Union*, *92*(4), 31. https://doi.org/10.1029/2011EO040003

Escher, C., & Gottstein, G. (1998). Nucleation of recrystallization in boron doped Ni3Al. *Acta Materialia*, *46*(2), 525–539. https://doi.org/10.1016/S1359-6454(97)00264-4

Fitz Gerald, J. D., & Stünitz, H. (1993). Deformation of granitoids at low metamorphic grade. I: Reactions and grain size reduction. *Tectonophysics*, *221*(3–4), 269–297. https://doi.org/10.1016/0040-1951(93)90163-E

Gandais, M., & Willaime, C. (1984). Mechanical properties of feldspars. In Brown, W. L. (Ed.), *Feldspars and Feldspathoids* NATO ASI Series (Series C: Mathematical and Physical Sciences) (Vol. 137, pp. 207–246). Dordrecht: Springer. https://doi.org/10.1007/978-94-015-6929-3_6

Gardner, R. L., Piazolo, S., Daczko, N. R., & Trimby, P. (2020). Microstructures reveal multistage melt present strain localisation in mid-ocean gabbros. *Lithos*, *366–367*, 105572. https://doi.org/10.1016/j.lithos.2020.105572

Hansen, L. N., Cheadle, M. J., John, B. E., Swapp, S. M., Dick, H. J. B., Tucholke, B. E., & Tivey, M. A. (2013). Mylonitic deformation at the Kane oceanic core complex: Implications for the rheological behavior of oceanic detachment faults: Rheology of Kane Oceanic Core Complex. *Geochemistry, Geophysics, Geosystems*, *14*(8), 3085–3108. https://doi.org/10.1002/ggge.20184

Harigane, Y., Michibayashi, K., & Ohara, Y. (2008). Shearing within lower crust during progressive retrogression: Structural analysis of gabbroic rocks from the Godzilla Mullion, an oceanic core complex in the Parece Vela backarc basin. *Tectonophysics*, *457*(3–4), 183–196. https://doi.org/10.1016/j.tecto.2008.06.009

Harigane, Y., Michibayashi, K., & Ohara, Y. (2011). Deformation and hydrothermal metamorphism of gabbroic rocks within the Godzilla Megamullion, Parece Vela Basin, Philippine Sea. *Lithos*, *124*(3–4), 185–199. https://doi.org/10.1016/j.lithos.2011.02.001

Hay, R. S., & Evans, B. (1987). Chemically induced grain boundary migration in calcite: Temperature dependence, phenomenology, and possible applications to geologic systems. *Contributions to Mineralogy and Petrology*, *97*(1), 127–141. https://doi.org/10.1007/BF00375220

Hirth, G., & Tullis, J. (1992). Dislocation creep regimes in quartz aggregates. *Journal of Structural Geology*, *14*(2), 145–159. https://doi.org/10.1016/0191-8141(92)90053-Y

Hirth, G., & Tullis, J. (1994). The brittle-plastic transition in experimentally deformed quartz aggregates. *Solid Earth*, *99*(B6), 11731–11747. https://doi.org/10.1029/93JB02873

Homburg, J. M., Hirth, G., & Kelemen, P. B. (2010). Investigation of the strength contrast at the Moho: A case study from the Oman Ophiolite. *Geology*, *38*(8), 679–682. https://doi.org/10.1130/G30880.1

Hosford, A., Tivey, M., Matsumoto, T., Dick, H., Schouten, H., & Kinoshita, H. (2003). Crustal magnetization and accretion at the Southwest Indian Ridge near the Atlantis II fracture zone, 0–25 Ma. *Journal of Geophysical Research*, *108*(B3). https://doi.org/10.1029/2001JB000604

Ji, S. (2004). A generalized mixture rule for estimating the viscosity of solid-liquid suspensions and mechanical properties of polyphase rocks and composite materials. *Journal of Geophysical Research*, *109*(B10). https://doi.org/10.1029/2004JB003124

Ji, S., & Mainprice, D. (1990). Recrystallization and Fabric Development in Plagioclase. *The Journal of Geology*, *98*(1), 65–79. https://doi.org/10.1086/629375

Ji, S., Mainprice, D., & Boudier, F. (1988). Sense of shear in high-temperature movement zones from the fabric asymmetry of plagioclase feldspars. *Journal of Structural Geology*, *10*(1), 73–81. https://doi.org/10.1016/0191-8141(88)90129-0

Ji, S., Tongbin, S., Salisbury, M. H., Sun, S., Michibayashi, K., Zhao, W., et al. (2014). Plagioclase preferred orientation and induced seismic anisotropy in mafic igneous rocks. *Journal of Geophysical Research: Solid Earth*, *119*, 8064–8088. https://doi.org/10.1002/2014JB011352

Ji, S., Wirth, R., Rybacki, E., & Jiang, Z. (2000). High-temperature plastic deformation of quartz-plagioclase multilayers by layer-normal compression. *Journal of Geophysical Research*, *105*(B7), 16651–16664. https://doi.org/10.1029/2000JB900130

Jiang, Z., Prior, D. J., & Wheeler, J. (2000). Albite crystallographic preferred orientation and grain misorientation distribution in a low-grade mylonite: Implications for granular flow. *Journal of Structural Geology*, *22*(11–12), 1663–1674. https://doi.org/10.1016/S0191-8141(00)00079-1

Kenkmann, T., & Dresen, G. (2002). Dislocation microstructure and phase distribution in a lower crustal shear zone—An example from the Ivrea-Zone, Italy. *International Journal of Earth Sciences*, *91*(3), 445–458. https://doi.org/10.1007/s00531-001-0236-9

Kronenberg, A. K., & Shelton, G. L. (1980). Deformation microstructures in experimentally deformed Maryland diabase. *Journal of Structural Geology*, *2*(3), 341–353. https://doi.org/10.1016/0191-8141(80)90022-X

Kruse, R., Stünitz, H., & Kunze, K. (2001). Dynamic recrystallization processes in plagioclase porphyroclasts. *Journal of Structural Geology*, *23*(11), 1781–1802. https://doi.org/10.1016/S0191-8141(01)00030-X

Lloyd, G. E., Farmer, A. B., & Mainprice, D. (1997). Misorientation analysis and the formation and orientation of subgrain and grain boundaries. *Tectonophysics*, *279*(1–4), 55–78. https://doi.org/10.1016/S0040-1951(97)00115-7

MacLeod, C. J., Dick, H. J. B., Blum, P., & Expedition 360 Scientists. (2017). Southwest Indian ridge lower crust and moho. In *Proceedings of the International Ocean Discovery Program* (Vol. 360). College Station, TX: International Ocean Discovery Program. https://doi.org/10.14379/iodp.proc.360.2017

Mainprice, D., Bachmann, F., Hielscher, R., & Schaeben, H. (2015). Descriptive tools for the analysis of texture projects with large datasets using MTEX : Strength, symmetry and components. *Geological Society, London, Special Publications*, *409*(1), 251–271. https://doi.org/10.1144/SP409.8

Marshall, D. B., & McLaren, A. C. (1977). The direct observation and analysis of dislocations in experimentally deformed plagioclase feldspars. *Journal of Materials Science*, *12*(5), 893–903. https://doi.org/10.1007/BF00540970

McLaren, A. C., & Pryer, L. L. (2001). Microstructural investigation of the interaction and interdependence of cataclastic and plastic mechanisms in Feldspar crystals deformed in the semi-brittle field. *Tectonophysics*, *335*, 15. https://doi.org/10.1016/S0040-1951(01)00042-7

Mehl, L., & Hirth, G. (2008). Plagioclase preferred orientation in layered mylonites: Evaluation of flow laws for the lower crust. *Journal of Geophysical Research*, *113*(B5), B05202. https://doi.org/10.1029/2007JB005075

Miranda, E. A., Hirth, G., & John, B. E. (2016). Microstructural evidence for the transition from dislocation creep to dislocation-accommodated grain boundary sliding in naturally deformed plagioclase. *Journal of Structural Geology*, *92*, 30–45. https://doi.org/10.1016/j.jsg.2016.09.002

Miranda, E. A., & John, B. E. (2010). Strain localization along the Atlantis Bank oceanic detachment fault system, Southwest Indian Ridge. *Geochemistry, Geophysics, Geosystems*, *11*(4), 34. https://doi.org/10.1029/2009GC002646

Montardi, Y. A., & Mainprice, D. (1987). A transmission electron microscopie study of the natural plastic defonnation of calcic plagioclases (An 68–70). *Bulletin de Mineralogie*, *110*(1), 1–14. https://doi.org/10.3406/bulmi.1987.8022

Newton, M. S., & Kennedy, G. C. (1968). Jadeite, analcite, nepheline, and albite at high temperatures and pressures. *American Journal of Science*, *266*(8), 728–735. https://doi.org/10.2475/ajs.266.8.728

Nguyen, D., Morishita, T., Soda, Y., Tamura, A., Ghosh, B., Harigane, Y., et al. (2018). Occurrence of felsic rocks in oceanic gabbros from IODP Hole U1473A: Implications for evolved melt migration in the lower oceanic crust. *Minerals*, *8*(12), 583. https://doi.org/10.3390/min8120583

Nozaka, T., Akitou, T., Abe, N., & Tribuzio, R. (2019). Biotite in olivine gabbros from Atlantis Bank: Evidence for amphibolite-facies metasomatic alteration of the lower oceanic crust. *Lithos*, *348–349*, 105176. https://doi.org/10.1016/j.lithos.2019.105176

Okudaira, T., Jeřábek, P., Stünitz, H., & Fusseis, F. (2015). High-temperature fracturing and subsequent grain-size-sensitive creep in lower crustal gabbros: Evidence for coseismic loading followed by creep during decaying stress in the lower crust? *Journal of Geophysical Research: Solid Earth*, *120*(5), 3119–3141. https://doi.org/10.1002/2014JB011708

Okudaira, T., Shigematsu, N., Harigane, Y., & Yoshida, K. (2017). Grain size reduction due to fracturing and subsequent grain-size-sensitive creep in a lower crustal shear zone in the presence of a CO_2-bearing fluid. *Journal of Structural Geology*, *95*, 171–187. https://doi.org/10.1016/j.jsg.2016.11.001

Oliot, E., Goncalves, P., & Marquer, D. (2010). Role of plagioclase and reaction softening in a metagranite shear zone at mid-crustal conditions (Gotthard Massif, Swiss Central Alps): Strain localization in granitic rocks. *Journal of Metamorphic Geology*, *28*(8), 849–871. https://doi.org/10.1111/j.1525-1314.2010.00897.x

Oliot, E., Goncalves, P., Schulmann, K., Marquer, D., & Lexa, O. (2014). Mid-crustal shear zone formation in granitic rocks: Constraints from quantitative textural and crystallographic preferred orientations analyses. *Tectonophysics*, *612–613*, 63–80. https://doi.org/10.1016/j.tecto.2013.11.032

Olsen, T. S., & Kohlstedt, D. L. (1984). Analysis of dislocations in some naturally deformed plagioclase feldspars. *Physics and Chemistry of Minerals*, *11*(4), 153–160. https://doi.org/10.1007/BF00387845
Olsen, T. S., & Kohlstedt, D. L. (1985). Natural deformation and recrystallization of some intermediate plagioclase feldspars. *Tectonophysics*, *111*(1–2), 107–131. https://doi.org/10.1016/0040-1951(85)90067-8
Paterson, M. S. (1995). A theory for granular flow accommodated by material transfer via an intergranular fluid. *Tectonophysics*, *245*(3–4), 135–151. https://doi.org/10.1016/0040-1951(94)00231-W
Pettigrew, T. L., Casey, J. F., & Miller, D. J. (1999). *Proc. ODP, Init. Repts*. (p. 179). Retrieved From http://www-odp.tamu.edu/publications/179_IR/179TOC.HTM
Poirier, J. P. (1985). *Creep of crystals: High-temperature deformation processes in metals, ceramics and minerals*. Cambridge University Press.
Poirier, J. P., & Guillopé, M. (1979). Deformation induced recrystallization of minerals. *Bulletin de Mineralogie*, *102*(2), 67–74. https://doi.org/10.3406/bulmi.1979.7256
Ronov, A., & Yaroshevsky, A. (1969). Chemical composition of the Earth's crust. *GMS*, *13*, 37–57.
Rosenberg, C. L., & Stünitz, H. (2003). Deformation and recrystallization of plagioclase along a temperature gradient: An example from the Bergell tonalite. *Journal of Structural Geology*, *25*(3), 389–408. https://doi.org/10.1016/S0191-8141(02)00036-6
Ryan, W. B. F., Carbotte, S. M., Coplan, J. O., O'Hara, S., Melkonian, A., Arko, R., et al. (2009). Global multi-resolution topography synthesis. *Geochemistry, Geophysics, Geosystems*, *10*(3). https://doi.org/10.1029/2008GC002332
Rybacki, E., & Dresen, G. (2004). Deformation mechanism maps for feldspar rocks. *Tectonophysics*, *382*(3–4), 173–187. https://doi.org/10.1016/j.tecto.2004.01.006
Satsukawa, T., Ildefonse, B., Mainprice, D., Morales, L. F. G., Michibayashi, K., & Barou, F. (2013). A database of plagioclase crystal preferred orientations (CPO) and microstructures- implications for CPO origin, strength, symmetry and seismic anisotropy in gabbroic rocks. *Solid Earth*, *4*(2), 511–542. https://doi.org/10.5194/se-4-511-2013
Scandale, E., Gandais, M., & Willaime, C. (1983). Transmission electron microscopic study of experimentally deformed k-feldspar single crystals: The (010)[001], 0011/2[-110]1/2[-112] and(1-11)1/2[110] slip systems. *Physics and Chemistry of Minerals*, *9*(3–4), 182–187. https://doi.org/10.1007/BF00308376
Schmid, S. M. (1994). Textures of geological materials: Computer model predictions versus empirical interpretations based on rock deformation experiments and field studies. In Bunge, H. J., Siegesmund, S., Skrotzki, W., & Weber, K. (Eds.), *Texture of geological materials*. (pp. 279–301). Oberursel: Deutsch gesellschaft für materialkunde.
Simpson, C. (1985). Deformation of granitic rocks across the brittle-ductile transition. *Journal of Structural Geology*, *7*(5), 503–511. https://doi.org/10.1016/0191-8141(85)90023-9
Skemer, P., Katayama, I., Jiang, Z., & Karato, S. (2005). The misorientation index: Development of a new method for calculating the strength of lattice-preferred orientation. *Tectonophysics*, *411*(1–4), 157–167. https://doi.org/10.1016/j.tecto.2005.08.023
Smith, J. V. (1984). Phase relations of plagioclase feldspars. In Brown, W. L. (Ed.), Feldspars and Feldspathoids (Series C: Mathematical and Physical Sciences) (Vol. 137, pp. 55–94). Dordrecht: Springer. https://doi.org/10.1007/978-94-015-6929-3_2
Stünitz, H. (1998). Syndeformational recrystallization—Dynamic or compositionally induced? *Contributions to Mineralogy and Petrology*, *131*(2–3), 219–236. https://doi.org/10.1007/s004100050390
Stünitz, H., & Fitz Gerald, J. D. (1993). Deformation of granitoids at low metamorphic grade. II: Granular flow in albite-rich mylonites. *Tectonophysics*, *221*(3–4), 299–324. https://doi.org/10.1016/0040-1951(93)90164-F
Stünitz, H., Fitz Gerald, J. D., & Tullis, J. (2003). Dislocation generation, slip systems, and dynamic recrystallization in experimentally deformed plagioclase single crystals. *Tectonophysics*, *372*(3–4), 215–233. https://doi.org/10.1016/S0040-1951(03)00241-5
Svahnberg, H., & Piazolo, S. (2010). The initiation of strain localisation in plagioclase-rich rocks: Insights from detailed microstructural analyses. *Journal of Structural Geology*, *32*(10), 1404–1416. https://doi.org/10.1016/j.jsg.2010.06.011
Taufner, R., Viegas, G., Faleiros, F. M., Castellan, P., & Silva, R. (2021). Deformation mechanisms of granulite-facies mafic shear zones from Hole U1473A, Atlantis Bank, Southwest Indian Ridge (IODP Expedition 360). *Journal of Structural Geology*, *149*, 104380. https://doi.org/10.1016/j.jsg.2021.104380
Teagle, D. A. H., Ildefonse, B., Blum, P., & Expedition 335 Scientists. (2012). *Deep drilling of intact ocean crust: Harnessing past lessons to inform future endeavors*. Integrated Ocean Drilling Program. https://doi.org/10.2204/iodp.proc.335.2012
Trimby, P. W., Prior, D. J., & Wheeler, J. (1998). Grain boundary hierarchy development in a quartz mylonite. *Journal of Structural Geology*, *20*(7), 917–935. https://doi.org/10.1016/S0191-8141(98)00026-1
Tullis, J. (1983). Deformation of feldspars. In Ribbe, P. H. (Ed.), *Feldspar mineralogy* (pp. 297–323). Mineral Society of America. https://doi.org/10.1515/9781501508547-018
Tullis, J., & Yund, R. A. (1977). Experimental deformation of dry westerly granite. *Journal of Geophysical Research*, *82*(36), 5705–5718. https://doi.org/10.1029/JB082i036p05705
Tullis, J., & Yund, R. A. (1985). Dynamic recrystallization of feldspar: A mechanism for ductile shear zone formation. *Geology*, *13*, 238–241. https://doi.org/10.1130/0091-7613(1985)13<238:DROFAM>2.0.CO;2
Tullis, J., & Yund, R. A. (1987). Transition from cataclastic flow to dislocation creep of feldspar: Mechanisms and microstructures. *Geology*, *15*(7), 606–609. https://doi.org/10.1130/0091-7613(1987)15<606:TFCFTD>2.0.CO;2
Twiss, R. J. (1977). Theory and applicability of a recrystallized grain size paleopiezometer. In Wyss, M. (Ed.), *Stress in the Earth* (pp. 227–244). Birkhäuser, Basel: Contributions to Current Research in Geophysics (CCRG). https://doi.org/10.1007/978-3-0348-5745-1_13
Urai, J. L., Means, W. D., & Lister, G. S. (1986). Dynamic recrystallization of minerals. In Hobbs, B. E., & Heard, H. C. (Eds.), Geophysical Monograph Series (Vol. 36, pp. 161–199). Washington, D. C.: American Geophysical Union. https://doi.org/10.1029/GM036p0161
Wenk, H. R., & Christie, J. M. (1991). Comments on the interpretation of deformation textures in rocks. *Journal of Structural Geology*, *13*(10), 1091–1110. https://doi.org/10.1016/0191-8141(91)90071-P
Wheeler, J., Prior, D., Jiang, Z., Spiess, R., & Trimby, P. (2001). The petrological significance of misorientations between grains. *Contributions to Mineralogy and Petrology*, *141*(1), 109–124. https://doi.org/10.1007/s004100000225
Yoshinobu, A. S., & Hirth, G. (2002). Microstructural and experimental constraints on the rheology of partially molten gabbro beneath oceanic spreading centers. *Journal of Structural Geology*, *24*(6–7), 1101–1107. https://doi.org/10.1016/S0191-8141(01)00094-3
Yund, R. A., & Tullis, J. (1991). Compositional changes of minerals associated with dynamic recrystallizatin. *Contributions to Mineralogy and Petrology*, *108*(3), 346–355. https://doi.org/10.1007/BF00285942

References From the Supporting Information

Ague, D. M., Wenk, H. R., & Wenk, E. (1990). Deformation microstructures and lattice orientations of plagioclase in Gabbros from central Australia. In Duba, A. G., Durham, W. B., Handin, J. W., & Wang, H. F. (Eds.), Geophysical Monograph Series (Vol. 56, pp. 173–186). Washington, D. C.: American Geophysical Union. https://doi.org/10.1029/GM056p0173

Baratoux, L., Schulmann, K., Ulrich, S., & Lexa, O. (2005). Contrasting microstructures and deformation mechanisms in metagabbro mylonites contemporaneously deformed under different temperatures (c. 650°C and c. 750°C). *The Geological Society of London*, *243*, 97–125.

Barreiro, J. G., Lonardelli, I., Wenk, H. R., Dresen, G., Rybacki, E., Ren, Y., & Tomé, C. N. (2007). Preferred orientation of anorthite deformed experimentally in Newtonian creep. *Earth and Planetary Science Letters*, *264*(1–2), 188–207. https://doi.org/10.1016/j.epsl.2007.09.018

Barreiro, J. G., Wenk, H.-R., & Vogel, S. (2015). Texture and elastic anisotropy of a mylonitic anorthosite from the Morin Shear Zone (Quebec, Canada). *Journal of Structural Geology*, *71*, 100–111. https://doi.org/10.1016/j.jsg.2014.07.021

Cross, A. J. (2015). *Microstructural evolution under non-steady state deformation in mid-crustal ductile shear zones, (Doctoral dissertation)*. University of Otago. Retrieved from http://hdl.handle.net/10523/5608

Díaz-Azpiroz, M., Lloyd, G. E., & Fernández, C. (2011). Deformation mechanisms of plagioclase and seismic anisotropy of the Acebuches metabasites (SW Iberian massif). *Geological Society, London, Special Publications*, *360*(1), 79–95. https://doi.org/10.1144/SP360.5

Egydio-Silva, M., & Mainprice, D. (1999). Determination of stress directions from plagioclase fabrics in high grade deformed rocks (Além Paraíba shear zone, Ribeira fold belt, southeastern Brazil). *Journal of Structural Geology*, *21*(12), 1751–1771. https://doi.org/10.1016/S0191-8141(99)00121-2

Egydio-Silva, M., Vauchez, A., Bascou, J., & Hippertt, J. (2002). High-temperature deformation in the Neoproterozoic transpressional Ribeira belt, southeast Brazil. *Tectonophysics*, *352*(1–2), 203–224. https://doi.org/10.1016/S0040-1951(02)00197-X

Fukuda, J., & Okudaira, T. (2013). Grain-size-sensitive creep of plagioclase accompanied by solution–precipitation and mass transfer under mid-crustal conditions. *Journal of Structural Geology*, *51*, 61–73. https://doi.org/10.1016/j.jsg.2013.03.006

Gandais, M., & Willaime, C. (1984). Mechanical properties of feldspars. In Brown, W. L. (Ed.), *Feldspars and Feldspathoids* NATO ASI Series (Series C: Mathematical and Physical Sciences) (Vol. 137, pp. 207–246). Dordrecht: Springer. https://doi.org/10.1007/978-94-015-6929-3_6

Hansen, L. N., Cheadle, M. J., John, B. E., Swapp, S. M., Dick, H. J. B., Tucholke, B. E., & Tivey, M. A. (2013). Mylonitic deformation at the Kane oceanic core complex: Implications for the rheological behavior of oceanic detachment faults: Rheology of Kane Oceanic Core Complex. *Geochemistry, Geophysics, Geosystems*, *14*(8), 3085–3108. https://doi.org/10.1002/ggge.20184

Heidelbach, F., Post, A., & Tullis, J. (2000). Crystallographic preferred orientation in albite samples deformed experimentally by dislocation and solution precipitation creep. *Journal of Structural Geology*, *22*(11–12), 1649–1661. https://doi.org/10.1016/S0191-8141(00)00072-9

Homburg, J. M., Hirth, G., & Kelemen, P. B. (2010). Investigation of the strength contrast at the Moho: A case study from the Oman Ophiolite. *Geology*, *38*(8), 679–682. https://doi.org/10.1130/G30880.1

Jensen, L. N., & Starkey, J. (1985). Plagioclase microfabrics in a ductile shear zone from the Jotun Nappe, Norway. *Journal of Structural Geology*, *7*(5), 527–539.

Jerabek, P., Stünitz, H., Heilbronner, R., Lexa, O., & Schulmann, K. (2007). Microstructural-deformation record of an orogen-parallel extension in the Vepor Unit, West Carpathians. *Journal of Structural Geology*, *29*(11), 1722–1743. https://doi.org/10.1016/j.jsg.2007.09.002

Ji, S. (2004). A generalized mixture rule for estimating the viscosity of solid-liquid suspensions and mechanical properties of polyphase rocks and composite materials. *Journal of Geophysical Research*, *109*(B10). https://doi.org/10.1029/2004JB003124

Ji, S., & Mainprice, D. (1988). Natural deformation fabrics of plagioclase: Implications for slip systems and seismic anisotropy. *Tectonophysics*, *147*(1–2), 145–163. https://doi.org/10.1016/0040-1951(88)90153-9

Ji, S., & Mainprice, D. (1990). Recrystallization and Fabric Development in Plagioclase. *The Journal of Geology*, *98*(1), 65–79. https://doi.org/10.1086/629375

Ji, S., Jiang, Z., Rybacki, E., Wirth, R., Prior, D., & Xia, B. (2004). Strain softening and microstructural evolution of anorthite aggregates and quartz–anorthite layered composites deformed in torsion. *Earth and Planetary Science Letters*, *222*(2), 377–390. https://doi.org/10.1016/j.epsl.2004.03.021

Ji, S., Mainprice, D., & Boudier, F. (1988). Sense of shear in high-temperature movement zones from the fabric asymmetry of plagioclase feldspars. *Journal of Structural Geology*, *10*(1), 73–81. https://doi.org/10.1016/0191-8141(88)90129-0

Ji, S., Wirth, R., Rybacki, E., & Jiang, Z. (2000). High-temperature plastic deformation of quartz-plagioclase multilayers by layer-normal compression. *Journal of Geophysical Research*, *105*(B7), 16651–16664. https://doi.org/10.1029/2000JB900130

Ji, S., Zhao, X., Zhao, P., de Grologie, D., & de Montrral (1994). On the measurement of plagioclase lattice preferred orientations. *Journal of Structural Geology*, *16*(12), 1711–1718. https://doi.org/10.1016/0191-8141(94)90136-8

Jiang, Z., Prior, D. J., & Wheeler, J. (2000). Albite crystallographic preferred orientation and grain misorientation distribution in a low-grade mylonite: Implications for granular flow. *Journal of Structural Geology*, *22*(11–12), 1663–1674. https://doi.org/10.1016/S0191-8141(00)00079-1

Kanagawa, K., Shimano, H., & Hiroi, Y. (2008). Mylonitic deformation of gabbro in the lower crust: A case study from the Pankenushi gabbro in the Hidaka metamorphic belt of central Hokkaido, Japan. *Journal of Structural Geology*, *30*(9), 1150–1166. https://doi.org/10.1016/j.jsg.2008.05.007

Kendrick, J. E., Lavallée, Y., Mariani, E., Dingwell, D. B., Wheeler, J., & Varley, N. R. (2017). Crystal plasticity as an indicator of the viscous-brittle transition in magmas. *Nature Communications*, *8*(1), 1926. https://doi.org/10.1038/s41467-017-01931-4

Kruhl, J. H. (1987). Preferred lattice orientations of plagioclase from amphibolite and greenschist facies rocks near the Insubric Line (Western Alps). *Tectonophysics*, *135*, 233–242.

Kruse, R., & Stünitz, H. (1999). Deformation mechanisms and phase distribution in mafic high-temperature mylonites from the Jotun Nappe, southern Norway. *Tectonophysics*, *303*(1–4), 223–249. https://doi.org/10.1016/S0040-1951(98)00255-8

Kruse, R., Stünitz, H., & Kunze, K. (2001). Dynamic recrystallization processes in plagioclase porphyroclasts. *Journal of Structural Geology*, *23*(11), 1781–1802. https://doi.org/10.1016/S0191-8141(01)00030-X

Lafrance, B., John, B. E., & Scoates, J. S. (1996). Syn-emplacement recrystallization and deformation microstructures in the Poe Mountain anorthosite, Wyoming. *Contributions to Mineralogy and Petrology*, *122*(4), 431–440. https://doi.org/10.1007/s004100050139

Lapworth, T., Wheeler, J., & Prior, D. J. (2002). The deformation of plagioclase investigated using electron backscatter diffraction crystallographic preferred orientation data. *Journal of Structural Geology*, *24*(2), 387–399. https://doi.org/10.1016/S0191-8141(01)00057-8

MacLeod, C. J., Dick, H. J. B., Blum, P., & Expedition 360 Scientists. (2017). Southwest Indian ridge lower crust and moho. In *Proceedings of the International Ocean Discovery Program* (Vol. 360). College Station, TX: International Ocean Discovery Program. https://doi.org/10.14379/iodp.proc.360.2017

Marshall, D. B., & McLaren, A. C. (1977a). Deformation mechanisms in experimentally deformed plagioclase feldspars. *Physics and Chemistry of Minerals*, *1*(4), 351–370.
Marshall, D. B., & McLaren, A. C. (1977b). The direct observation and analysis of dislocations in experimentally deformed plagioclase feldspars. *Journal of Materials Science*, *12*(5), 893–903. https://doi.org/10.1007/BF00540970
Mehl, L., & Hirth, G. (2008). Plagioclase preferred orientation in layered mylonites: Evaluation of flow laws for the lower crust. *Journal of Geophysical Research*, *113*(B5), B05202. https://doi.org/10.1029/2007JB005075
Michibayashi, K., Harigane, Y., Ohara, Y., Muto, J., & Okamoto, A. (2014). Rheological properties of the detachment shear zone of an oceanic core complex inferred by plagioclase flow law: Godzilla Megamullion, Parece Vela back-arc basin, Philippine Sea. *Earth and Planetary Science Letters*, *408*, 16–23. https://doi.org/10.1016/j.epsl.2014.10.005
Miranda, E. A., Hirth, G., & John, B. E. (2016). Microstructural evidence for the transition from dislocation creep to dislocation-accommodated grain boundary sliding in naturally deformed plagioclase. *Journal of Structural Geology*, *92*, 30–45. https://doi.org/10.1016/j.jsg.2016.09.002
Montardi, Y. A., & Mainprice, D. (1987). A transmission electron microscopie study of the natural plastic defonnation of calcic plagioclases (An 68–70). *Bulletin de Mineralogie*, *110*(1), 1–14. https://doi.org/10.3406/bulmi.1987.8022
Oliot, E., Goncalves, P., Schulmann, K., Marquer, D., & Lexa, O. (2014). Mid-crustal shear zone formation in granitic rocks: Constraints from quantitative textural and crystallographic preferred orientations analyses. *Tectonophysics*, *612–613*, 63–80. https://doi.org/10.1016/j.tecto.2013.11.032
Olsen, T. S., & Kohlstedt, D. L. (1984). Analysis of dislocations in some naturally deformed plagioclase feldspars. *Physics and Chemistry of Minerals*, *11*(4), 153–160. https://doi.org/10.1007/BF00387845
Olsen, T. S., & Kohlstedt, D. L. (1985). Natural deformation and recrystallization of some intermediate plagioclase feldspars. *Tectonophysics*, *111*(1–2), 107–131. https://doi.org/10.1016/0040-1951(85)90067-8
Pearce, F. D., Rondenay, S., Sachpazi, M., Charalampakis, M., & Royden, L. H. (2012). Seismic investigation of the transition from continental to oceanic subduction along the western Hellenic Subduction Zone. *Journal of Geophysical Research*, *117*(B7). https://doi.org/10.1029/2011JB009023
Prasannakumar, V., & Lloyd, G. (2007). Development of crystal lattice preferred orientation and seismic properties in Bhavani shear zone, Southern India. *Journal of the Geological Society of India*, *70*(282–296), 26.
Rosenberg, C. L., & Stünitz, H. (2003). Deformation and recrystallization of plagioclase along a temperature gradient: An example from the Bergell tonalite. *Journal of Structural Geology*, *25*(3), 389–408. https://doi.org/10.1016/S0191-8141(02)00036-6
Scandale, E., Gandais, M., & Willaime, C. (1983). Transmission electron microscopic study of experimentally deformed k-feldspar single crystals: The (010)[001], 0011/2[-110]1/2[-112] and(1-11)1/2[110] slip systems. *Physics and Chemistry of Minerals*, *9*(3–4), 182–187. https://doi.org/10.1007/BF00308376
Shigematsu, N., & Tanaka, H. (2000). Dislocation creep of ®ne-grained recrystallized plagioclase under low-temperature conditions. *Journal of Structural Geology*, *22*(1), 65–79. https://doi.org/10.1016/S0191-8141(99)00132-7
Siegesmund, S., Helming, K., & Kruse, R. (1994). Complete texture analysis of a deformed amphibolite: Comparison between neutron diffraction and U-stage data. *Journal of Structural Geology*, *16*(1), 131–142. https://doi.org/10.1016/0191-8141(94)90024-8
Stünitz, H., Fitz Gerald, J. D., & Tullis, J. (2003). Dislocation generation, slip systems, and dynamic recrystallization in experimentally deformed plagioclase single crystals. *Tectonophysics*, *372*(3–4), 215–233. https://doi.org/10.1016/S0040-1951(03)00241-5
Svahnberg, H., & Piazolo, S. (2010). The initiation of strain localisation in plagioclase-rich rocks: Insights from detailed microstructural analyses. *Journal of Structural Geology*, *32*(10), 1404–1416. https://doi.org/10.1016/j.jsg.2010.06.011
Terry, M. P., & Heidelbach, F. (2006). Deformation-enhanced metamorphic reactions and the rheology of high-pressure shear zones, Western Gneiss Region, Norway. *Journal of Metamorphic Geology*, *24*(1), 3–18. https://doi.org/10.1111/j.1525-1314.2005.00618.x
White, J. C. (1990). Albite deformation within a basal ophiolite shear zone. *Geological Society, London, Special Publications*, *54*(1), 327–333. https://doi.org/10.1144/GSL.SP.1990.054.01.29
Xie, Y., Wenk, H. -R., & Matthies, S. (2003). Plagioclase preferred orientation by TOF neutron diffraction and SEM-EBSD. *Tectonophysics*, *370*(14), 269–286. https://doi.org/10.1016/S0040-1951(03)00191-4